Metamorphic bedrock geometry of Santorini using HVSR information and geophysical modeling of ambient noise and active-source surface-wave data

Nikos Chatzis [a,*], Costas Papazachos [a], Nikos Theodoulidis [b], Panagiotis Hatzidimitriou [a],
Georgios Vougioukalakis [c], Michele Paulatto [d], Ben Heath [e], Emilie Hooft [e], Douglas Toomey [e],
Marios Anthymidis [a], Chrisa Ventouzi [a]

[a] Geophysical Laboratory, Aristotle University of Thessaloniki, Greece
[b] Institute of Engineering Seismology & Earthquake Engineering (EPPO-ITSAK), Thessaloniki, Greece
[c] Hellenic Authority of Geology & Mineral Surveys, E.A.G.M.E., Athens, Greece
[d] Department of Earth Science and Engineering, Imperial College London, London, UK
[e] Department of Earth Sciences, University of Oregon, Eugene, OR, USA

A B S T R A C T

Santorini is the most active volcano of the Southern Aegean Volcanic Arc, with volcanic material that has accumulated during the last 600+ Kyrs on top of the pre-volcanic Santorini island. The geometry of the pre-volcanic basement not only provides constraints on the volcanic history, but is also fundamental for seismic hazard assessment, as it partly controls site-effects on strong ground motions. We investigate the geometry of the metamorphic (Cycladic) basement of Santorini using information from both passive (noise) and active source data. We performed a large number (~280) of single-station ambient noise measurements and collected additional data from 42 previous studies to compute the Horizontal-to-Vertical Spectral Ratio (HVSR) curves. The majority of the recovered HVSR curves show prominent spectral ratio peaks (locally larger than 7–8) indicating a large impedance contrast between pyroclastic volcanic strata and bedrock metamorphic formations. We also performed active (MASW) and passive (Noise Array) surface wave measurements at 4 selected sites to determine local dispersion curves. To find the 1D Vs structure from the surface down to the metamorphic bedrock we performed a joint Monte Carlo inversion of the dispersion curves and the fundamental frequency (f_0^{HVSR}) values from the HVSR curves. These models, as well as deep borehole information and HVSR data along the caldera cliff, where the thickness and stratigraphy of the volcanic formations above the bedrock can be directly observed, allowed us to determine a linear relationship between the thickness of the pyroclastic formations and their fundamental resonance period for central-southern Santorini. The resulting geometry of pre-volcanic island shows deep basins around the pre-Alpine bedrock outcrop (Profitis Ilias) and generally agrees with recent results from larger-scale tomographic and gravity data but with some significant local differences. The basins are 200+ meters thick in the Kamari and Perissa area (southeastern Santorini) and >400 m thick in the central (Fira-Imerovigli) area, while there is a thick (~70-130 m) pyroclastic layer on top of a metamorphic basement "plateau" in the Megalochori area.

1. Introduction

The Santorini island (Fig. 1) is the most significant active volcano of the southern Aegean area (southern Greece). While being part of the Hellenic (Southern Aegean) Volcanic Arc, it is also part of the Cyclades islands, a large complex of islands dominated by metamorphic basement geology. The volcanism in the southern Aegean is associated with

subduction of the Eastern Mediterranean plate beneath the Aegean microplate (Le Pichon and Angelier, 1979), as well as the NW-SE Miocene extension phase of the Aegean (Bohnhoff et al., 2006). The broader area is also associated with significant seismotectonic activity, as demonstrated by the 9th July 1956 M7.5 mainshock, the strongest shallow earthquake event in Europe during the 20th century, which occurred along the major NW-SE Santorini-Amorgos Fault Zone. This
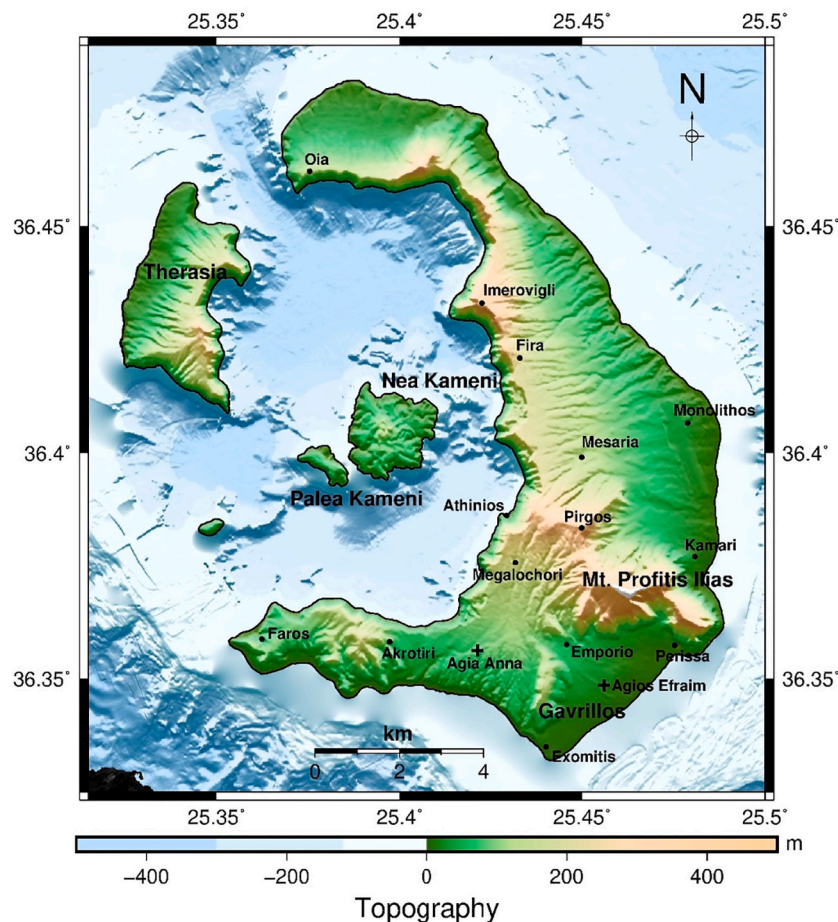

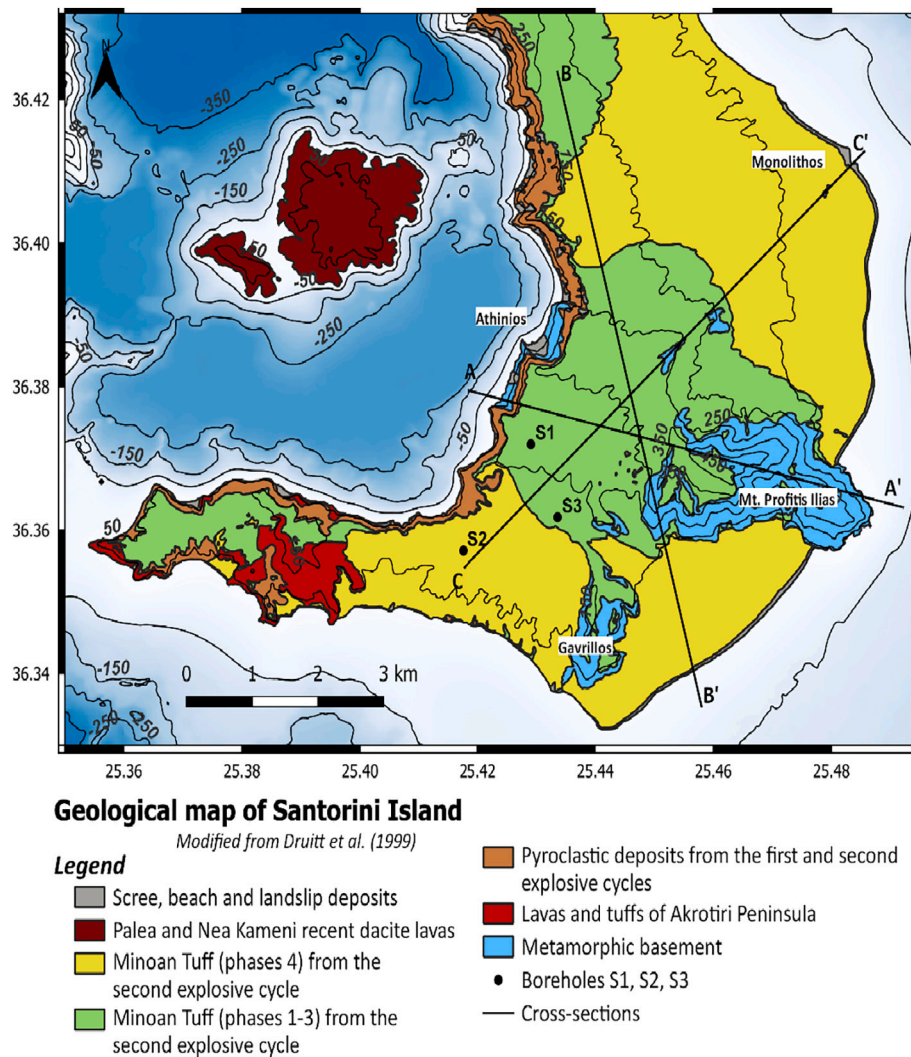**Fig. 1.** Topographic map of the Santorini island complex.

event resulted in heavy damage in Santorini (Papazachos and Papazachou, 2003), with high macroseismic intensities at Oia, Fira, Imerovigli (VIII+), Megalogori, and Pirgos (VIII).

Volcanic activity in the Santorini area started before ~650Kyrs (Druitt et al., 1999), producing hundreds of meters of lavas and pyroclastic deposits. These deposits filled the pre-existing basins of the pre-volcanic metamorphic basement of Santorini, forming the present Santorini island. Improved knowledge of the basement geometry is a key factor for the understanding Santorini's volcanic history. It allows us to estimate the overall thickness of the two main cycles of volcanic deposits (e.g., Druitt et al., 1999) above bedrock. Moreover, it allows us to study the tectonic deformation and active faulting that contributed to the development of the present basement geometry, since regional deformation controls the faults within the metamorphic basement (e.g., Budetta et al., 1984; Perissoratis, 1995) that in turn shape the bedrock morphology. The metamorphic basement of Santorini is thought to be part of the broader Attico-Cycladic complex and was exhumed during a Miocene (and likely also more recent) extensional phase (e.g., Piper and Perissoratis, 2003; Piper et al., 2007).

The bedrock geometry, as well as the structure (thickness and elastic properties) of the overlying volcanic formations, play a critical role in site-effect studies in Santorini, and are needed for reliable seismic hazard assessments. This is evidenced by the impact of the M7.5 1956 Amorgos mainshock, which caused heavy damage to the island of Santorini. The available modified Mercalli intensities (Papazachos et al., 1997) suggest significant spatial variability of the damage distribution, as the reported intensity values range from 6 to 8+. While this variability has been shown (Kkallas et al., 2018) to be partly controlled by topographic effects for the caldera rim settlements (e.g., Oia, Fira, Imerovigli, etc.), significantly increased damage was also observed for settlements around the Profitis Ilias mountain (Megalochori, Pyrgos, Episkopi, etc.). It is plausible to assume that the high contrast of the pyroclastic volcanics and the underlying bedrock resulted in significant local amplifications, which controlled and contributed to the described damage pattern. This underlines the necessity to improve knowledge of the Santorini bedrock-volcanics geometry.

Ambient noise methods have been extensively used during the last three decades for site-effect investigation. One of the most frequently employed methods is the Horizontal to Vertical Spectral Ratio technique (HVSR, Nogoshi and Igarashi, 1971; Nakamura, 1989), which provides a reliable estimate of the resonance frequency (f_0) of sedimentary (and other similar) formations above bedrock. Though many studies use the HVSR method (e.g., Moisidi et al., 2015; Papadopoulos et al., 2017; Kula et al., 2018; Cheng et al., 2021) due to its low cost and fast application in the field, its theoretical background is still in debate. Bonnefoy-Claudet et al. (2006a, 2006b, 2008) showed theoretically that the fundamental frequency estimated by this approach, f_0^{HVSR}, is practically equal to the S-wave resonant frequency, f_0, as well as the peak frequency, f_0^{ell}, of the Rayleigh-wave ellipticity for 1D homogeneous models with high-to-moderate impedance contrast between the bedrock and shallower formations. Furthermore, Haghshenas et al. (2008) verified the good agreement between f_0^{HVSR} and the f_0 estimates obtained with the SSR technique (Borcherdt, 1970) by using data from several studies worldwide. The same authors have also showed that the maximum HVSR amplitude provides a lower limit of the actual maximum spectral amplification amplitude, as this is identified in the SSR curves. The previous observations verify the usefulness of the HVSR technique for the determination of the resonant frequency and the spectral

Geological map of Santorini Island

Modified from Druitt et al. (1999)

Legend

- Scree, beach and landslip deposits
- Palea and Nea Kameni recent dacite lavas
- Minoan Tuff (phases 4) from the second explosive cycle
- Minoan Tuff (phases 1-3) from the second explosive cycle
- Pyroclastic deposits from the first and second explosive cycles
- Lavas and tuffs of Akrotiri Peninsula
- Metamorphic basement
- • Boreholes S1, S2, S3
- — Cross-sections

Fig. 2. Simplified geological map of the central-southern Santorini Island (modified from Druitt et al., 1999). The main morphology contours are also depicted. The locations of the cross-sections A-A', B-B' and C-C', as well as of deep boreholes S1, S2 and S3, are also shown.

amplification of S-waves due to the local site effects.

Based on these observations, the HVSR technique is frequently applied for the determination of the S-wave fundamental frequency, f_0, in microzonation studies, as well as for rapid mapping of the sedimentary formation thickness, h, above the bedrock. This is usually done using the quarter-wavelength approximation, $h = V_S/4*f_0$, where V_S is the average shear-wave velocity of the sediments above bedrock. The sediment V_S profiles can be directly estimated through borehole measurements (e.g., crosshole and downhole data) or from active and passive surface wave methods such as Multichannel Analysis of Surface Waves, MASW, (Park et al., 1999) and ambient noise array data (Foti et al., 2018), which capture the dispersion characteristics of the Rayleigh-waves (Aki, 1957; Capon, 1969). While the determined dispersion curves are usually inverted independently for the local 1D V_S model, joint inversion approaches (e.g., dispersion and HVSR curve inversion) have also been used (Arai and Tokimatsu, 2005) providing more accurate Vs models for cases with moderate-to-large bedrock depths (typically >30 m).

Ambient noise geophysical surveys have been successfully applied in volcanic environments, usually employing HVSR and surface-wave dispersion data (e.g., Chávez-García et al., 2007; Nardone and Maresca, 2011). Leyton et al. (2013) collected HVSR data at the Talca and Curicó cities (central Chile) after heavy damage caused by the very large Maule earthquake (M8.8, 2010); they found prominent HVSR peaks for the areas of Talca city which is underlain by volcanic ash deposits and a good agreement between HVSR results and the extent of damage in those parts of the city. Panzera et al. (2019) investigated the structure of the parasitic pyroclastic cone of Mt. Vetore (Mt. Etna volcano) with the use of single-station and array ambient noise data, showing that the joint inversion of both data types allowed to obtain a reliable shear-wave velocity profile of the cone. Recently, Torrese et al. (2020) explored the application of a joint active/passive seismic survey for the stratigraphic investigation of planetary volcanic analogues, using the Tinguatón volcano (Canary islands) as a test site. They demonstrated that the combined interpretation of active and passive seismic data allowed to determine a preliminary 2D model of the subsurface geophysical/geological structure, mapping the main volcanic units, i.e., scoria deposits, different basaltic lava flows, etc.

In the present work we estimate the thickness of pyroclastic volcanics above the metamorphic basement in central-southern Santorini using information from both passive (ambient noise) and active seismic sources. Recently, Tzanis et al. (2020) proposed a model for Santorini's pre-volcanic Alpine basement using gravity data. They used average densities for the pyroclastic formations, older volcanics (first cycle), and bedrock from previous studies and performed a stripping inversion analysis on an updated local gravity anomaly map to produce the morphology of the bottom of the pyroclastic layer, as well as of the pre-volcanic Alpine basement. Moreover, P-wave tomographic results by
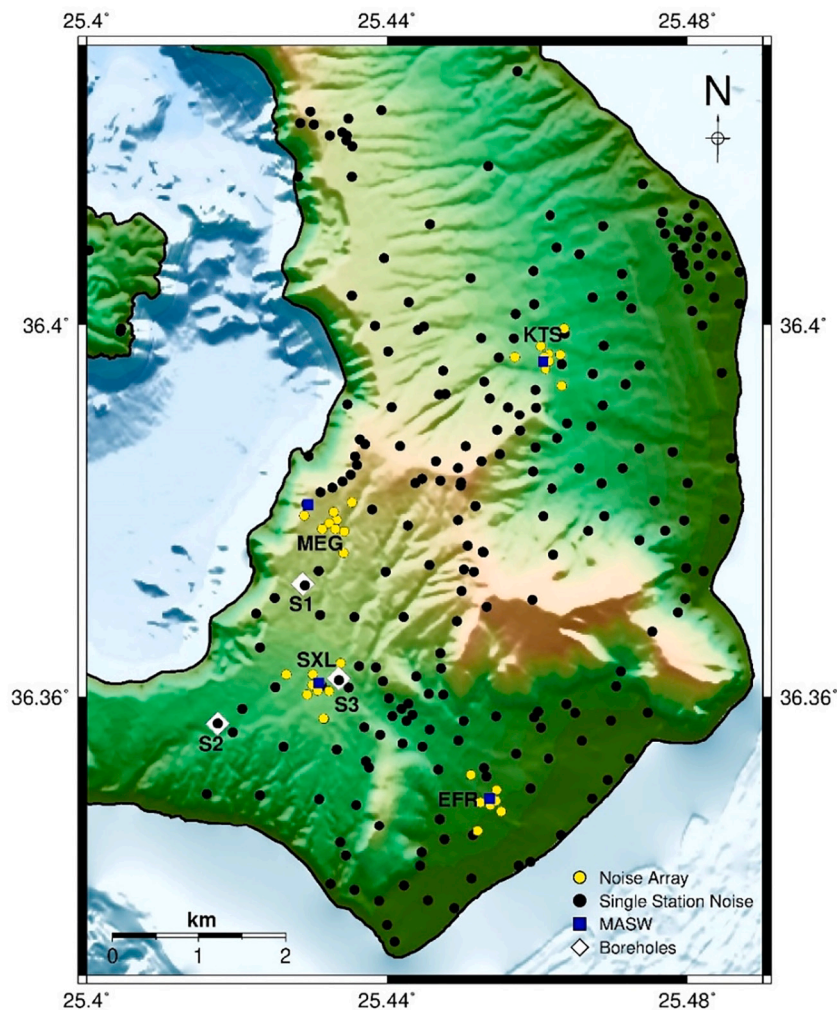
Fig. 3. Locations of 281 single-station ambient noise measurement sites and the 42 additional sites that were processed in this study (black dots. Passive Noise Array station and active MASW locations at the four examined sites (EFR, SXL, MEG, and KTS) are depicted with yellow dots and blue squares, respectively. Deep boreholes reaching the metamorphic basement (S1, S2, and S3) are shown with white diamonds. (For interpretation of the references to colour in this figure legend, the reader is referred to the web version of this article.)

Heath et al. (2019), determined using data from the PROTEUS (2015) imaging experiment (https://santorini.uoregon.edu/), provided new constraints on the metamorphic basement geometry of the broader Santorini area, especially regarding the sub-marine continuation of the Santorini metamorphic basement in the broader area around Santorini.

2. Santorini geology and volcanism

The geology of Santorini is characterized by the presence of its pre-Alpine metamorphic basement (pre-volcanic island), which is overlain by numerous volcanic deposits. Fig. 2 presents a simplified geological map (modified from Druitt et al., 1999) for the central-southern part of Santorini, which is the focus of this study. The basement units consist of schists and crystalline limestones (Skarpelis and Liati, 1990) that are typical of the Cycladic islands' metamorphic basement (Andriessen et al., 1987). The schists are metapelites, meta-sandstones, and meta-volcanic formations of Palaeocene-Eocene age (Tataris, 1964), while the limestones are of upper-Triassic age (Papastamatiou, 1956). Two main Alpine metamorphic events are seen in the basement units (Altherr et al., 1979; Andriessen et al., 1979), namely an Eocene high-pressure (blueschist-facies) and an overprinted Miocene medium-pressure (greenschist-facies) metamorphism. Schists are found in the Athinios port area and on the caldera walls. Other basement outcrop sites consist of limestones (with local schist interlayering), found in mount Profitis Ilias and the Gavrillos ridge. A granitic intrusion has also been observed in a single deep borehole (Fytikas et al., 1990; Skarpelis and Liati, 1990) with skarn formations at the limestone contact. The present shape of the

metamorphic basement in Santorini island is the result of multiple extension episodes that caused the Aegean crust to collapse and formed the Cyclades islands (included Santorini). The extension started from the Oligocene-Miocene in a WNW-ESE direction and continues to the present in a roughly NW-SE direction (e.g., Mercier et al., 1989; Bohnhoff et al., 2006; Jolivet et al., 2013).

According to Druitt et al. (1999), the Akrotiri Peninsula volcanic rocks are the oldest deposits above the pre-Alpine basement and include the Early Volcanic Centers (650-550 ka) and the Cinder Cones (450-340 ka). The Early Volcanic Centers mostly consist of submarine domes with rhyodacitic, dacitic, and andesitic lavas and rhyodacite pumice tuffs, while Cinder Cones consist of basaltic and andesitic lavas that overlie the Early Volcanic Centers rocks. Extensive pyroclastic deposits have been produced by at least 12 major eruptions of the first (360-180 ka) and second (180–3.6 ka) explosive cycles of Santorini. During the first explosive cycle, five large explosive eruptions and two lavas successions took place, with the last two explosive eruptions believed to be of Plinian intensity. The explosive eruptions produced five andesitic-rhyodacitic pyroclastic and pumice-fall deposits. Andesitic and rhyodacitic lavas are placed between the pyroclastic deposits but are found mostly to the north (between Mesaria and Fira); these are considered as a single geological unit in the current study. Seven large explosive eruptions took place during the second explosive cycle, with several of them being Plinian. Six of the largest eruptions produced andesitic, dacitic, and rhyodacitic pyroclastics and pumice-fall deposits. Lavas are also found in this second cycle (e.g., rhyodacites of Therasia, andesites of Oia), but are outside our study area (Fig. 2).

Table 1

Small- (ARRAY01) and large-aperture (ARRAY02) Noise Array configurations at the four (4) measurement sites in Santorini (bad. Rec. indicates problematic records).

Radii	ARRAY01 10 Stations at:				ARRAY02 10 Stations at:			
	0 m	15 m	50 m	150 m	0 m	50 m	150 m	400 m
EFR	1	5 + 1 bad rec.	3	–	1	3	3	2 + 1 bad rec.
SXL	1	6	3	–	1	2 + 1 bad rec.	3	3
MEG	1	3	3	3	1	3	3	3
KTS	1	3	3	3	1	3	3	3

The latest large explosive eruption of the second cycle took place during the Late Bronze Age (LBA eruption ~1610 BCE, Baillie and Munro, 1988; Friedrich et al., 2006, Friedrich et al., 2014; Manning et al., 2014) and is known as the Minoan eruption. Recent results for carbon dating of olive trees (Ehrlich et al., 2021) suggest that later dates (~1560 BCE), compatible with archaeological evidence (e.g., Höflmayer, 2012) are also possible. The Minoan eruption formations are shown as two units in Fig. 2, namely the tuffs of Phases 1–3 and the rhyodacitic ignimbrites (also described as Minoan tuffs) of Phase 4. The main eruption began with Phase 1 of Plinian intensity producing rhyodacitic pumice deposits. Phreatomagmatic explosions took place during Phases 2 and 3, producing several tens of meters of tuffs. Recent dacitic lava volcanism continues at the new volcanic centers of Palea and Nea Kameni since 197 BCE with the most recent eruption in 1950 CE. The present Santorini caldera was formed by at least four large collapse episodes (Druitt, 2014) during the first and second explosive cycles, creating a few-hundred-meter caldera cliff, in which the Minoan and pyroclastic deposits, as well as the underlying basement formation in the Athinios port area, are well observed. This long eruptive history of Santorini volcanic island has built up a complex series of volcanic layers over the original metamorphic pre-Alpine basement.

3. Geophysical data and methods

We performed an extensive geophysical survey in Santorini, using surface wave data from passive and active sources, to determine the metamorphic bedrock geometry beneath the volcanic formations. The survey focused around the Profitis Ilias mountain (Figs. 1 and 2) due to the relatively simple geology, which consists of pyroclastic formations above basement, without significant lateral variations. Moreover, the relatively "shallow" bedrock depth (<300 m) allows the application of ambient noise methods. A large number (~280, Fig. 3) of single-station ambient noise measurements were performed with Guralp-40 T/30s seismometers and RefTek-130 digitizers. The duration of the noise recordings varied between 1.5 and 3 h at each site. Moreover, 42 additional noise records for the broader Santorini island were collected during the PROTEUS experiment in 2005, from the temporary stations installed by Dimitriadis et al. (2009), as well as from the permanent stations of the Hellenic Unified Seismic Networks (FDSN codes HT, HL, HA, and HC).

We also conducted four passive Noise Array and active MASW measurements to determine the Rayleigh dispersion curves (DC) for the estimation of the local 1D Vs model. These four sites were located in volcanic basins around Profitis Ilias and are depicted in Fig. 3 with yellow dots and blue squares, respectively (Agios Efraim church [EFR], Emporio nursery school [SXL], Megalochori [MEG], and Koutsogiannopoulos Santorini Wine Museum [KTS]). For the ambient noise arrays, we used ten broadband Guralp-6TD/20s seismometers, conducting two sets of measurements at each site, with a smaller (ARRAY01) and a large (ARRAY02) aperture, to record higher- and lower-frequency surface waves (see Table 1 for details). More than 2 hours and 12 hours of noise records were collected for the ARRAY01 and ARRAY02 configurations, respectively. MASW data were also collected with a StrataView (Geometrics) digitizer, a 7Kg sledgehammer source, and 24 vertical 4.5 Hz geophones along ~100 m profiles. These data were collected at or very close to the center of the noise arrays to allow joint surface wave DC processing and interpretation. A typical configuration for the acquisition of both data types for the site of Agios-Efraim (EFR) is shown in Fig. 4.
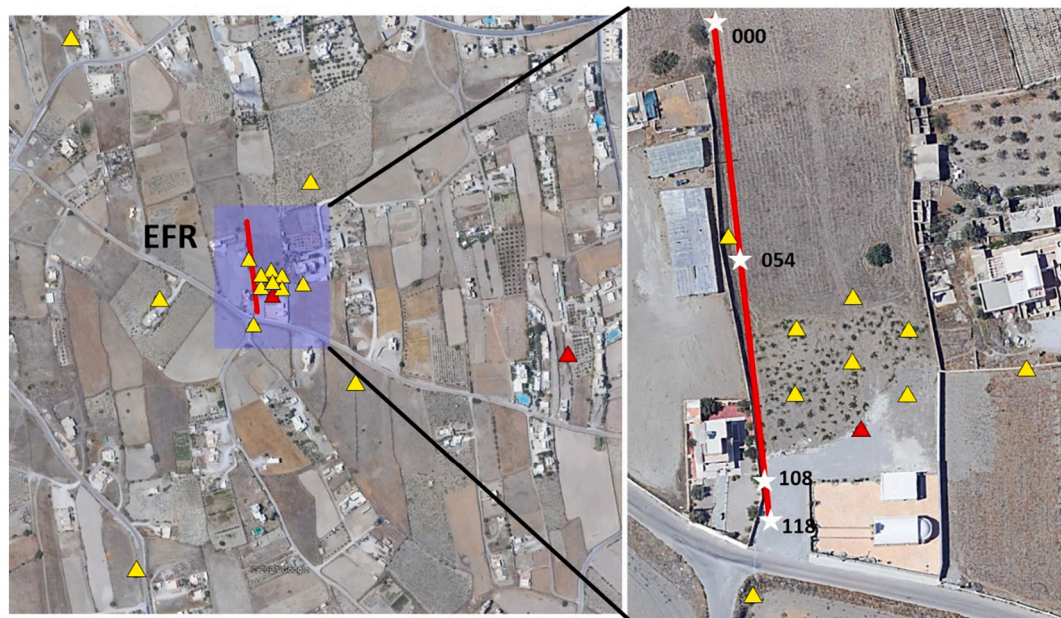
Fig. 4. Typical configuration for Noise Array (passive) and MASW (active) measurements from the Agios-Efraim (EFR) site. Nine seismographs (triangles, left figure) were placed at an average radius of 50, 150, and 400 m from a central recording station (see Table 1). Red triangles show two rejected sites (acquisition failure). The right figure shows the MASW profile (red solid line) and four shot locations (white stars at 0, 54, 108, and 118 m along the profile). (For interpretation of the references to colour in this figure legend, the reader is referred to the web version of this article.)
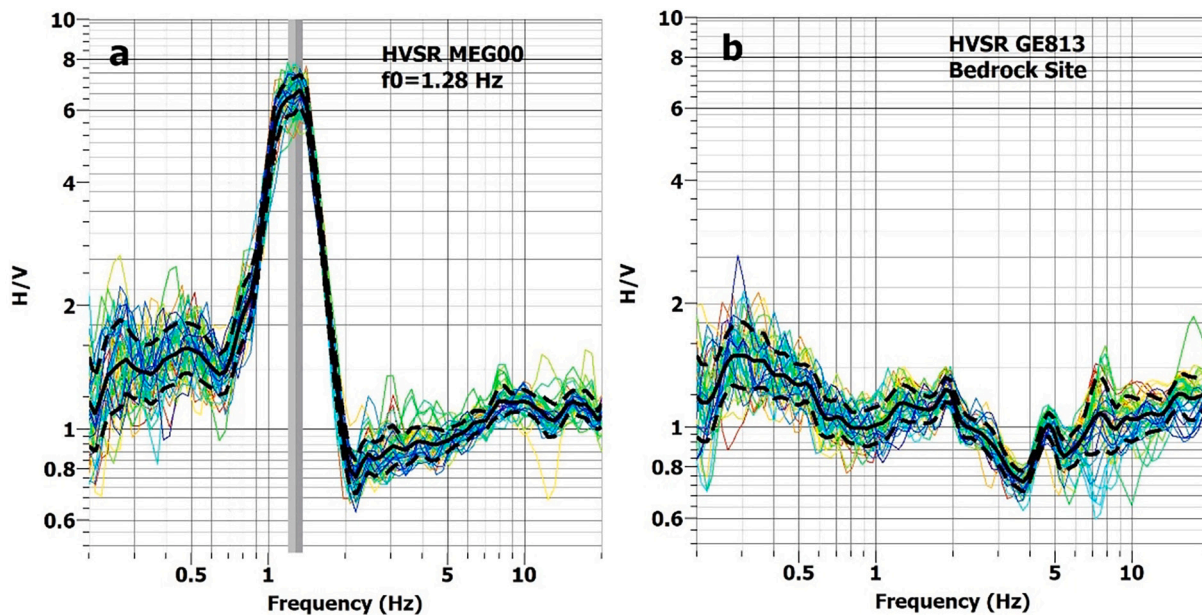
Fig. 5. Selected average HVSR curves (solid lines) and their uncertainty (dashed lines), computed from the individual HVSR curves (colored lines) of each ambient noise record window: (a) A prominent single peak ($A_0^{HVSR} > 6$) HVSR curve for the Megalochori area (central station of noise array MEG), indicating a strong impedance contrast between the metamorphic bedrock and the volcanic pyroclastic formations (fundamental frequency, $f_0^{HVSR} = 1.28$ Hz). (b) Typical flat HVSR curve for the GE813 Profitis Ilias bedrock site.
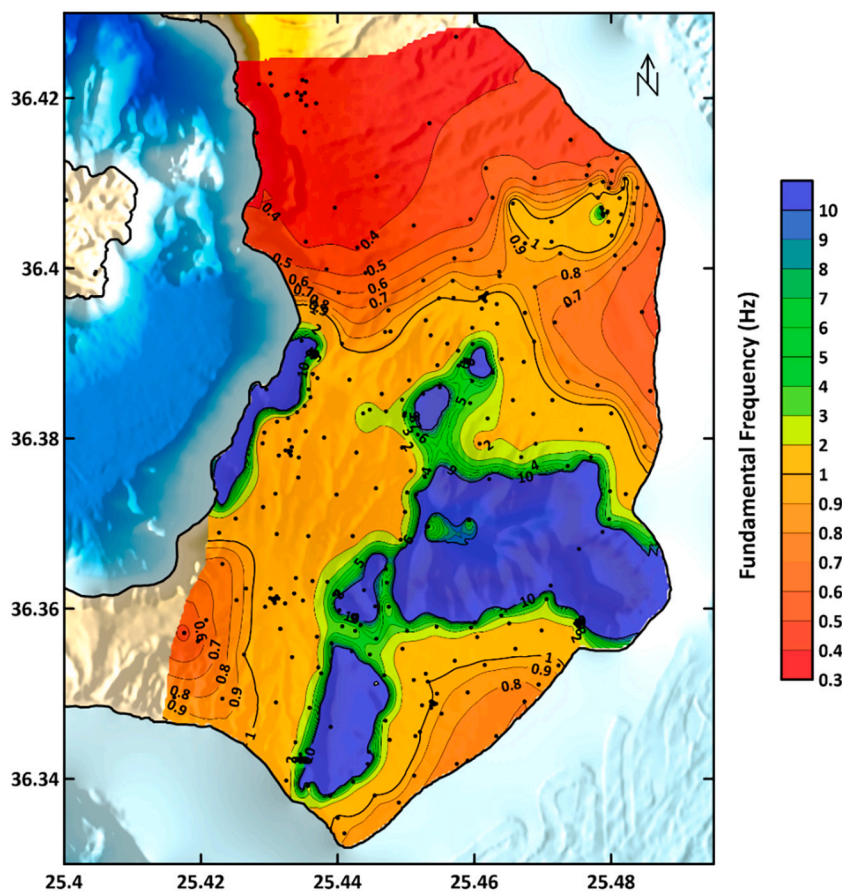
Fig. 6. Contour map of the variation of the fundamental frequency (f_0^{HVSR}) for central-southern Santorini determined from HVSR data (measurement sites are shown with black dots).
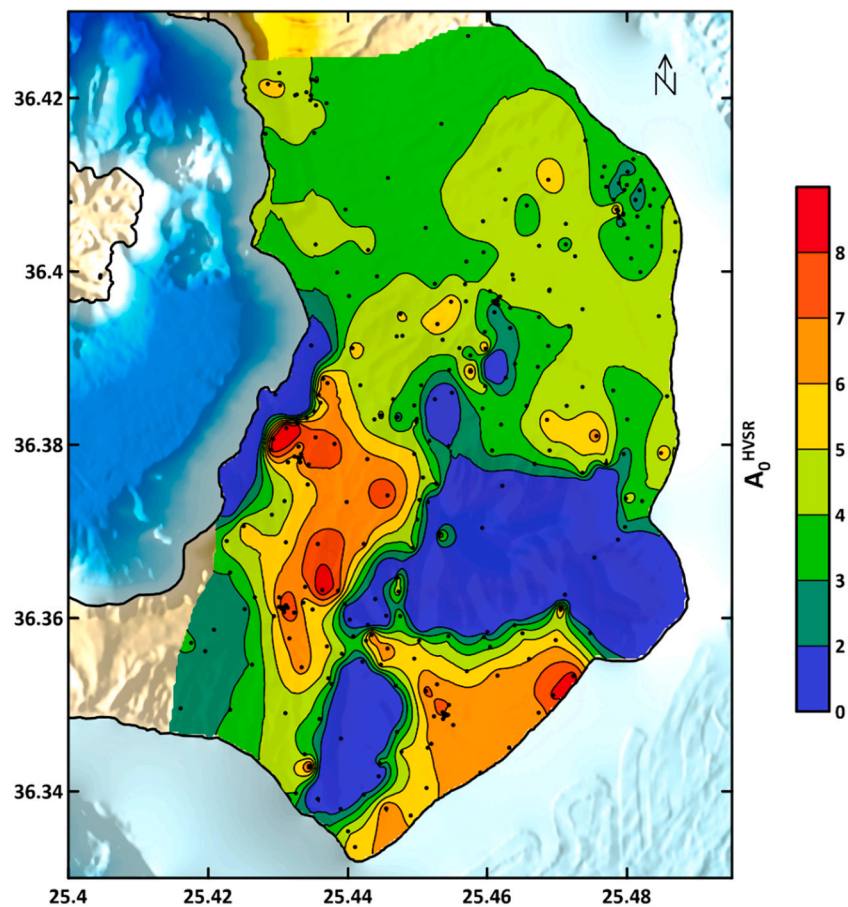
Fig. 7. Contour map of the variation of the maximum amplitude of the HVSR curves (A_0^{HVSR}) for central-southern Santorini (measurement sites are shown with black dots).
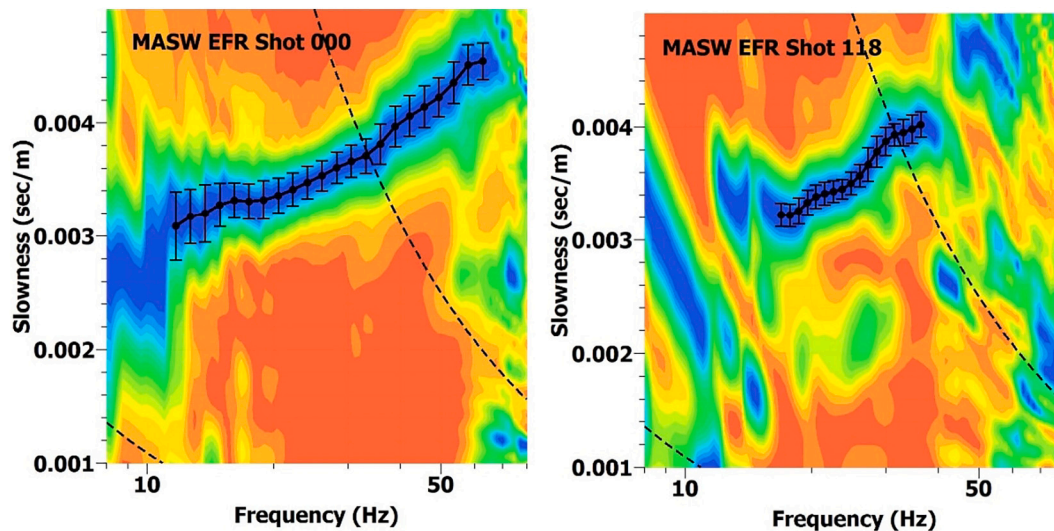

Fig. 8. Slowness-frequency amplitude plots for shots at 0 and 118 m along the MASW profile at array site EFR. The picked phase velocity dispersion curve, as well as its uncertainty, is shown with a solid line. Lower and upper slowness limits for each frequency are shown with dashed lines (see text for details).

3.1. Single-station Horizontal-to-Vertical Spectral Ratio (HVSR) information for Santorini

The Horizontal-to-Spectral-Ratio (HVSR) method was applied to all available (~320) single-station noise data. All data were processed with the GEOPSY software (www.geopsy.org, Wathelet, 2005; Wathelet

et al., 2020), which computes the HVSR spectral ratio of the squared average horizontal components over the vertical component for selected time windows (duration 60–200 s, depending on the record's duration and the f_0 value of each site). The final HVSR curves were computed by averaging more than 20 time-windows, applying a Konno and Ohmachi (1998) log-frequency smoothing filter with a b-value of 40. HVSR
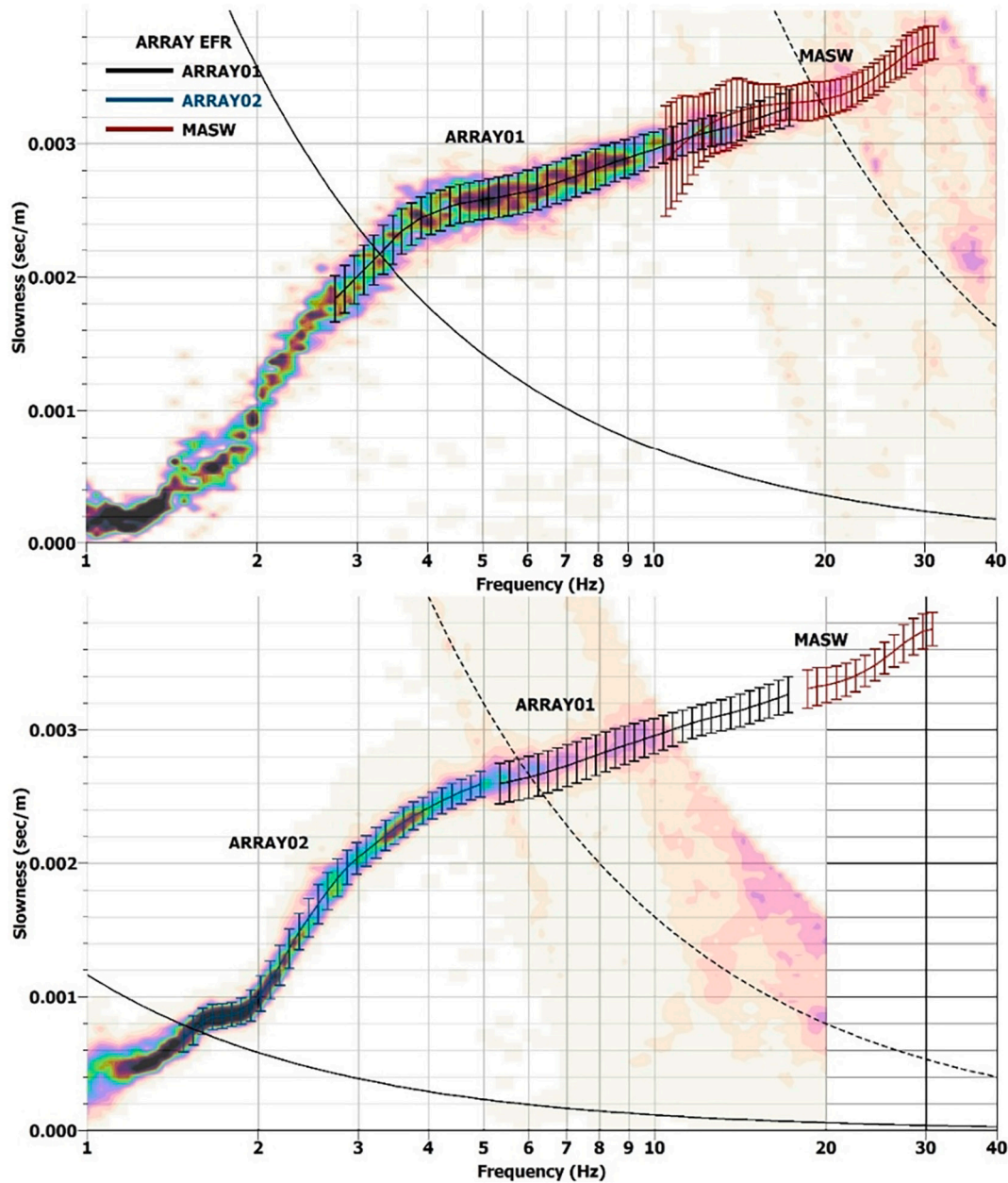
Fig. 9. Slowness-frequency amplitude plots and Rayleigh-waves phase slowness dispersion results for the ARRAY01 (top) and ARRAY02 (bottom) configurations at the EFR site (see Table 1). The corresponding MASW dispersion curve is plotted in red in both plots. The picked dispersion curves from ARRAY01 (data in top image), and ARRAY02 (data in bottom image) are plotted with black and blue lines, respectively, in the bottom image. The lower (S_{min}) and upper (S_{max}) slowness resolution limits are shown with a black solid and dashed lines, respectively. (For interpretation of the references to colour in this figure legend, the reader is referred to the web version of this article.)

processing was performed following the SESAME project guidelines (Bard, 2008).

In Fig. 5 we present two typical HVSR curves, from a site in Megalochori (Minoan tuffs and other pyroclastic deposits, Fig. 5a) as well as a typical metamorphic bedrock site (Profitis Ilias limestone, Fig. 5b). The pattern at the Megalochori site is representative of most stations at pyroclastic sites, with the HVSR curve exhibiting a very clear, single prominent peak, with large (>4) maximum amplitudes (noted as A_0^{HVSR}), and fundamental frequencies, f_0^{HVSR}, in the range 0.5–1.5 Hz. Such large amplitude HVSR peaks are indicative of the strong impedance contrast between the underlying metamorphic bedrock and the surficial, slower (smaller Vs) and less dense volcanic (pyroclastic) formations. On the contrary, the bedrock site in Fig. 5b shows a rather flat HVSR curve, with a maximum spectral value <2, similar to what is normally expected for

bedrock sites.

Figs. 6 and 7 depict the spatial distribution of the fundamental frequency, f_0^{HVSR}, and the corresponding maximum HVSR amplitude, A_0^{HVSR}, from the 323 measurements of Fig. 3. All sites for which the HVSR curve was rather flat ($A_0^{HVSR} < \sim 2$), were considered "bedrock" sites, as proposed by the SESAME guidelines (Bard, 2008). For presentation purposes, we assigned a unit maximum amplitude and an arbitrary high frequency of 20 Hz to all bedrock areas (Profitis Ilias and Gavrillos mounts, as well as Athinios harbor). Both figures suggest the presence of significant variability in the HVSR results and the corresponding f_0^{HVSR} and A_0^{HVSR} values across this part of Santorini. More specifically:

Dispersion curve and fundamental frequency joint inversion (EFR)
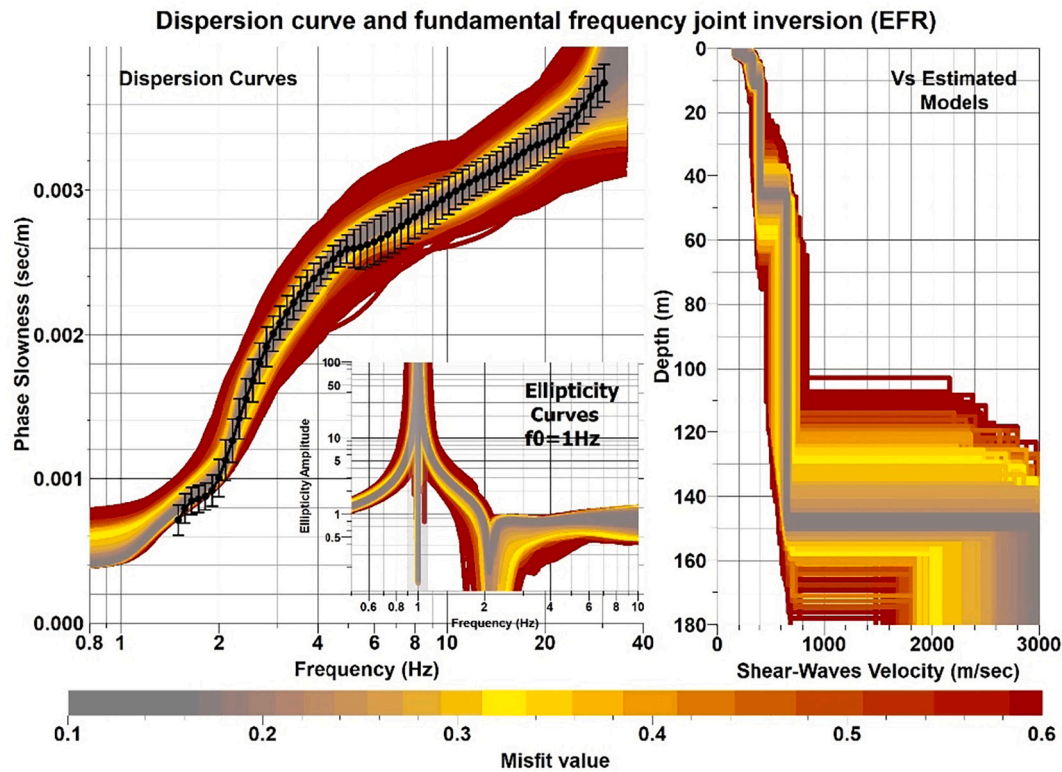
Fig. 10. Joint dispersion curve (DC) and fundamental frequency (f_0) inversion results for the EFR site. (Left) Observed (black solid line) and simulated model (colored) dispersion curves. In the inset figure the corresponding simulated ellipticity curves show peaks very close to the $f_0^{HVSR} = 1$ Hz value determined from the HVSR data. (Right) Vs models (colored curves) generated from the neighborhood algorithm inversion procedure. All curves are colored according to the joint misfit (colour scale).

a) Sites located on pyroclastic formations between the metamorphic outcrops of Profitis Ilias, Gavrilos, and Athinios port (see Figs. 1 and 2 for locations), show single-peak HVSR curves with large A_0^{HVSR} values (>4), similar to Fig. 5a, and f_0^{HVSR} values in the range 0.7-2 Hz. For these sites, the low density/low-Vs pyroclastics are placed directly on top of the metamorphic bedrock formations, resulting in a high-impedance contrast, and giving rise to the large A_0^{HVSR} values. The same pattern is also observed in the Perissa basin (SE Santorini), where the geological setting is similar.

b) Moving towards the southwest, where the Akrotiri formations are found between the pyroclastics and the bedrock (Fig. 2), we observe lower fundamental frequencies ($f_0^{HVSR} \sim 0.5$ Hz), indicating a thickness increase of the volcanic formations above the bedrock. At the same time, the A_0^{HVSR} values drop significantly, with local values <3. This pattern is consistent with the smaller impedance contrast expected between the pyroclastics and the underlying Akrotiri lavas and tuffs, as discussed later.

c) Moving to the north, the HVSR curves become more complex with double-peaked curves. In the broader Fira area, they show low fundamental frequencies ($f_0^{HVSR} \sim 0.3$–0.4Hz) indicative of a large volcanic formation thickness. To the northeast, where a small limestone outcrop is observed at Monolithos (see Fig. 2), similar but more complex double peak HVSR curves are observed. While the resonant peak frequencies are higher in this area (~1 Hz) compared to Fira, they also exhibit significant peaks at relatively low frequencies, showing no similarity to the Profitis Ilias and Athinios "flat" bedrock HVSR curves. This suggests a more complicated bedrock-volcanic stratigraphy near the Monolithos bedrock outcrop.

To further quantify the previous qualitative findings, we include additional information on the 3D geometry of the bedrock and volcanic formations including metamorphic bedrock depth derived either from direct observations (deep boreholes, stratigraphic observations on the caldera walls) or indirectly assessed from the available passive (noise Arrays) and active (MASW profiles) geophysical data.

3.2. Dispersion curve assessment from active and passive seismic data

Dispersion curves of Rayleigh waves were obtained from the ambient noise array and MASW profile surface-wave data at the 4 sites shown in Fig. 3 (EFR, SXL, MEG, and KTS). The typical data collection configuration is shown in Fig. 4. The two approaches are complementary. The active-source MASW method constrains the high frequency (typically above 5-10 Hz) part of the dispersion curve, providing improved resolution at shallow depths. The noise array can record ambient noise from passive sources over a broader frequency range providing the dispersion curve at lower frequencies (typically 1-15 Hz).

The MASW method (Park et al., 1999) was applied for each active source location using vertical-component Rayleigh-waves recordings. Dispersion curves (DC) were calculated with the f-k method (Capon, 1969; Yilmaz, 1987) implemented in the GEOPSY software package. For each frequency the minimum and maximum phase slowness, S_{min} and S_{max}, are controlled by the maximum and minimum recorded wavelengths, λ_{max} and λ_{min}, (Park and Carnevale, 2010; Foti et al., 2018), which are equal to the total profile length and twice the geophone spacing, respectively. Fig. 8 shows examples of picked dispersion curves (large amplitudes in the slowness-frequency domain, shown with blue colors) for shots at 0 m and 118 m at the EFR site (Fig. 4). While for both shots the dispersion curve extends well beyond the theoretical high-frequency limit, we used only the dispersion curve segments within the resolved range (dashed lines). The final dispersion curve is the average of all the individual dispersion curves at the four measurement sites (see Fig. 3 for locations).
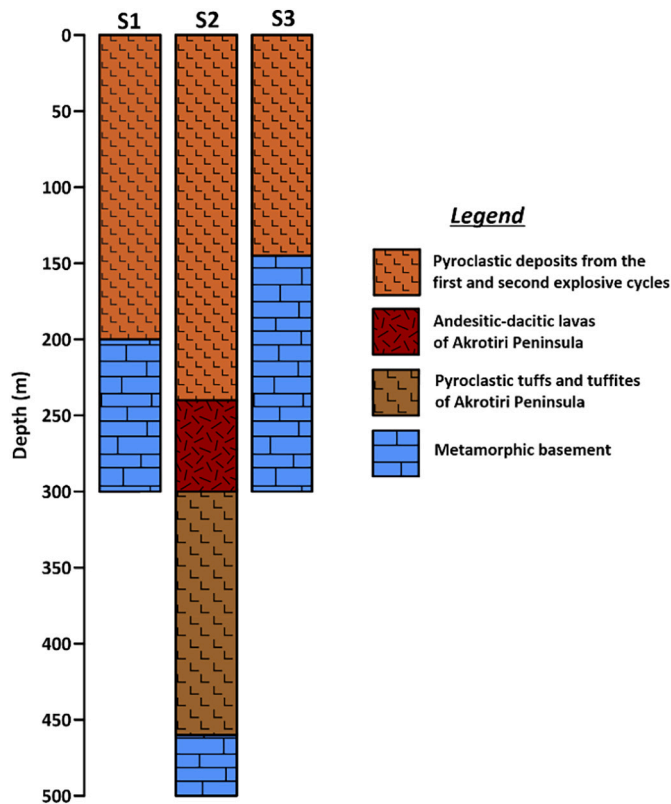
Fig. 11. Geological stratigraphy of three deep boreholes (S1, S2 and S3) in southern Santorini that penetrated the metamorphic bedrock (data from Fytikas et al., 1990).

For the noise arrays Rayleigh-wave phase slowness dispersion was computed using the generalized beamforming HRFK (High Resolution Frequency Wavenumber) algorithm (Capon, 1969), also implemented in the Geopsy package. Fig. 9 shows a typical example of the dispersion curve determination for the EFR site, showing the resulting dispersion images for the smaller and larger aperture configurations (ARRAY01 and ARRAY02, respectively, in Table 1) with the MASW dispersion curve superimposed. There is an excellent agreement between the MASW dispersion curve and both the smaller-aperture ARRAY01 dispersion curve (Fig. 9 top) and the larger-aperture ARRAY02 dispersion curve (Fig. 9 bottom). In both plots, the lower (S_{min}) and upper (S_{max}) slowness limits (Wathelet et al., 2008) are plotted with black solid and dashed lines, respectively. While the dispersion curve can be traced well below the theoretical lower frequency limit, as defined by the minimum slowness (S_{min}) curves, we did not employ the corresponding dispersion curve segment.

3.3. Joint inversion of the fundamental frequency and Rayleigh wave phase dispersion curves

To estimate 1D ground profiles of the shear-waves velocities, V_s, versus the depth at the four sites we performed a joint-inversion of the final dispersion curve with the fundamental frequency, f_0^{HVSR} at each site. For this reason, an average f_0^{HVSR} value and its standard deviation were computed for each noise array HVSR curve. All inversions were performed using a Monte Carlo neighborhood algorithm (Wathelet, 2008), which is included in the Dinver module of the Geopsy package software. Starting models for the inversion included 3 and 4 uniform layers over a homogeneous bedrock half-space, depending on the test site. The maximum bedrock depth, H, was allowed to vary from H/1.5 to H*2.5 and H was determined from the fundamental frequency, f_0, following Chatzis et al. (2018):

$$H = 81.9/f_0 \tag{1}$$

More than 50,000 test models were examined in the inversion. For each ground model the corresponding theoretical dispersion curve, fundamental frequency, and relative RMS misfits (Wathelet, 2005) between the theoretical and observed data were computed. For the dispersion curves, the misfit, is defined as:

$$Misfit_{DC} = \sqrt{\sum \left(\frac{DC_i^{obs} - DC_i^{sim}}{\sigma_i^{exp} * N} \right)^2} \tag{2}$$

where DC_i^{obs} and DC_i^{sim} are the observed and simulated (modeled) dispersion curve samples (phase velocities for each frequency), respectively, σ_i^{obs} the standard deviation of the observed samples, and N the total number of samples. For f_0^{HVSR}, the corresponding misfit is:

$$Misfit_{f_0} = \frac{f_0^{HVSR} - f_0^{sim}}{\sigma f_0^{HVSR}} \tag{3}$$

where f_0^{HVSR} and f_0^{sim} are the observed (from HVSR data) and modeled fundamental frequency, respectively, and σf_0^{HVSR} is the standard deviation of f_0^{HVSR}. For eq. (3) the f_0^{HVSR} values were considered to be equal to the frequency of the peak ellipticity ratio of the Rayleigh-waves that dominate the noise wavefield (e.g., Bonnefoy-Claudet et al., 2006b). We confirmed this by extracting the Rayleigh-wave ellipticity from the noise field using the RAYDEC algorithm (Hobiger et al., 2009), which resulted in practically identical f_0^{HVSR} values.

The Monte-Carlo search minimizes the joint misfit:

$$Misfit_{joint} = 0.5*Misfit_{DC} + 0.5*Misfit_{f_0} \tag{4}$$

where, in the absence of other information, equal weights are assigned to both measures of misfit. We performed several tests for the number of initial model layers, as well as for the joint inversion procedure and found that 3 to 4 layers were sufficient for good misfit minimization. For each layer, as well as the bedrock half-space, the S-wave velocities (which control both the DC and ellipticity information) were allowed to vary over a large range (150-3500 m/s). An example of the final joint inversion is given in Fig. 10 for site EFR. Each dispersion and ellipticity curve (left figure) correspond to a tested V_s model (right figure) with the colour depicting the joint misfit. The results show that identification of the bedrock depth from only the dispersion curves is a difficult task, as the Rayleigh-wave slowness continues to decrease for the lowest frequencies considered (~1–2 Hz). In the joint inversion employed here, the f_0^{HVSR} values provide constraints on the depth of the bedrock interface, while the dispersion curves recover the detailed S-wave velocity structure of the overlying volcanic layers.

The joint inversion results from the dispersion curves and the fundamental frequencies for the other three (3) array sites (MEG, SXL and KTS) are similar and provided in the Appendix 0. From the final models, the average shear-waves velocities from the surface up to the bedrock depth, V_{sz}, were 530 m/s (bedrock at 148 m) for site EFR, 566 m/s (bedrock at 124 m) for site MEG, 565 m/s (bedrock at 132 m) for site SXL, and 525 m/s (bedrock at 144 m) for site KTS. These rather similar average S-wave velocities (525-566 m/s) are representative of the pyroclastic formations above the metamorphic basement. Moreover, a shallow velocity discontinuity is observed at sites EFR and SXL (depths of 46 m and 34 m, respectively), with lower average Vs values in the overlying formation (373 m/s and 415 m/s, respectively). While this layer may correspond to the locally "softer" Minoan deposits, a similar observation for the MEG and KTS sites is absent, suggesting that locally the V_s profiles have difficulty separating the Minoan layer from older pyroclastic deposits.

3.4. Determination of the metamorphic bedrock geometry

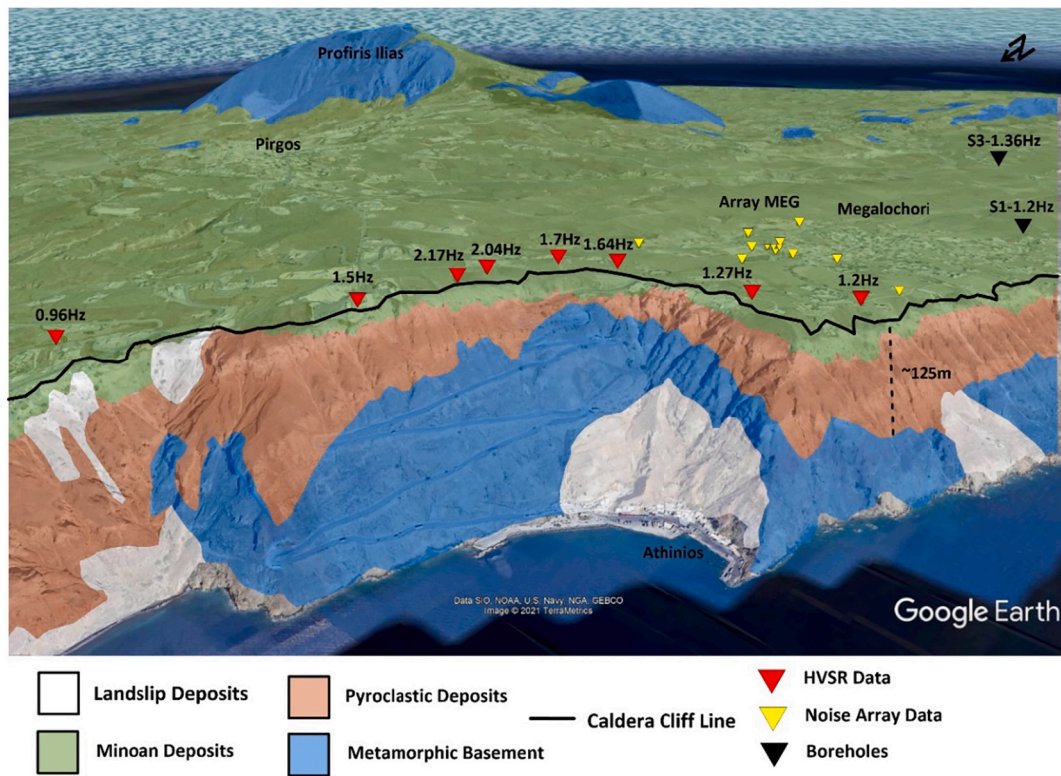The information at the four array sites allowed us to provide a

Fig. 12. Geological stratigraphy along the Santorini caldera wall and HVSR measurement sites (red triangles) along the caldera rim. In the Athinios area the thickness of pyroclastic formations (green and brown layers) above the basement (blue) can be directly observed. The nearby MEG ambient noise array stations and f_0 values for boreholes S1 and S3 are also shown with yellow and black triangles, respectively. Geology modified from Druitt et al. (1999). (For interpretation of the references to colour in this figure legend, the reader is referred to the web version of this article.)
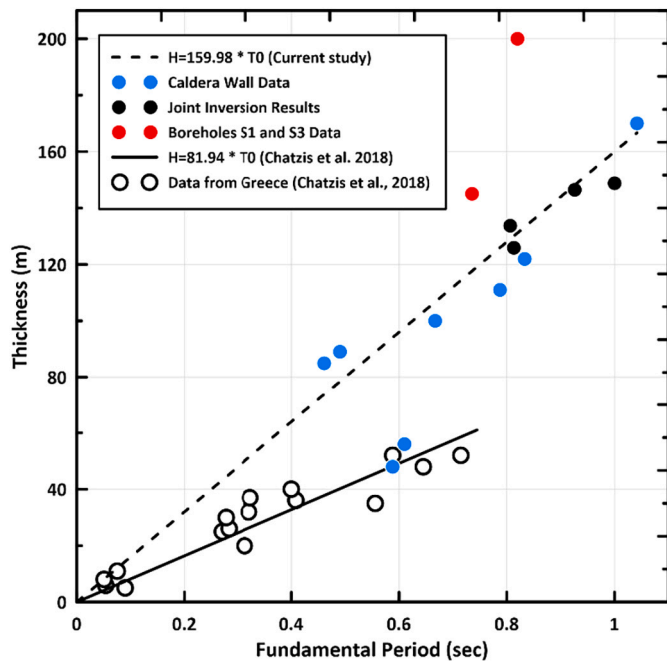

Fig. 13. Total pyroclastic formation thickness, H, versus the fundamental period, T_0^{HVSR}, for Santorini (solid circles). The best-fit through origin line (black dashed line) is also shown. The similar empirical equation of Chatzis et al. (2018) for Greek sedimentary basins, with the corresponding data (black solid line and open circles) are also plotted for comparison.

preliminary quantitative correlation between the bedrock depth and the HVSR frequency, f_0. To improve this correlation, we added independent information on the bedrock depth from two sources:

a) Three deep boreholes made by the Greek Geological Survey [IGME] (Fytikas et al., 1990) reached the metamorphic bedrock (see Figs. 2 and 3 for locations). Fig. 11 shows the geological stratigraphy of the cores using the classification from the map in Fig. 2. We obtained single-station noise records to estimate f_0^{HVSR} at each borehole.

b) The Santorini caldera walls allow direct observation of the local geology; hence the metamorphic bedrock depth can be quite easily measured. We performed eight HVSR measurements along the caldera rim, mainly above the Athinios port bedrock area (Fig. 12).

The pattern of the bedrock-pyroclastics interface observed in Fig. 12 provides additional information for the evaluation of the bedrock morphology. The first observation is that the interface exhibits rather complex, 3D variations, as seen by the very anomalous and strongly varying (within a few hundred meters) upper bedrock interface of Fig. 12. It is interesting to notice that while f_0^{HVSR} reaches higher values in the area where the bedrock is closer to the surface (1.64–2.17Hz) and decreases towards the north and south where the pyroclastics have larger thicknesses, the f_0^{HVSR} values show a rather smooth spatial variability, as they clearly "average" the small-scale strong variation of the underlying pyroclastics-bedrock boundary. On the other hand, the typical bedrock depth close to the Megalochori array is roughly 125 m, in very good agreement with the depth range (122-132 m) resulting from the joint DC-f_0^{HVSR} inversion approach (see Fig. A1 in Appendix 0).

Using all the available bedrock depth estimates (4 array sites, 8 caldera rim measurements, and 2 of the deep boreholes), we show in Fig. 13 the variation of the total volcanic thickness-bedrock depth, H, versus the fundamental period, T_0, from the HVSR results. While there is
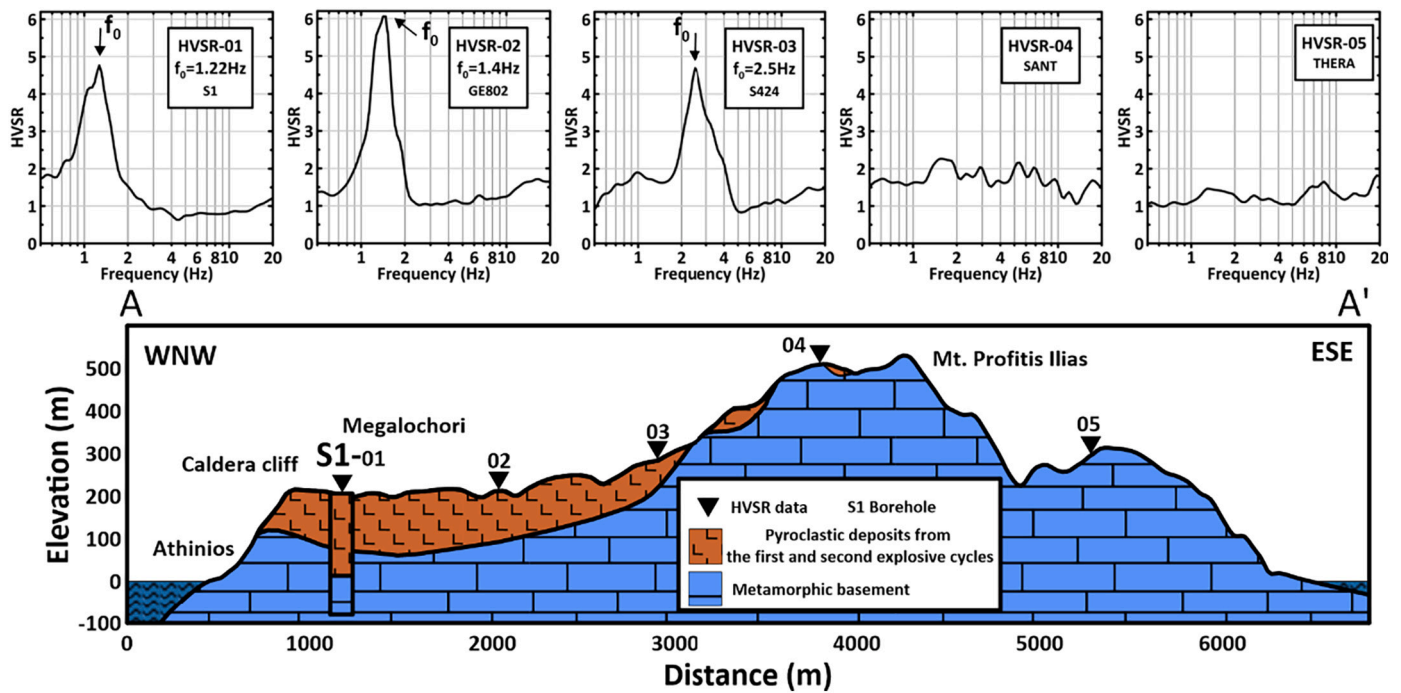
Fig. 14. Cross-section A-A' along Athinios, Megalochori and Mt. Profitis Ilias (see Fig. 2 for position). Indicative HVSR curves are displayed along the cross-section (measurement positions depicted with numbered triangles). The stratigraphy of borehole S1 is also shown (collocated with HVSR-01).

some scatter, a linear (running through origin) fit to the data:

$$H = 159.98 * T_o^{HVSR} = \frac{159.98}{f_o^{HVSR}} \qquad (5)$$

allows us to convert the HVSR f_0^{HVSR} values into bedrock depths. We have excluded information from borehole S2 in this plot, since it is not clear which formation (Akrotiri lavas or metamorphic bedrock, see Fig. 11) is responsible for the impedance contrast that leads to a low $f_0^{HVSR} = 0.47$ Hz value (derived from the HVSR data of the same site, see also discussion later). However, most of the caldera rim and array data follow the best-fit curve, except for two points located above the caldera rim, where the local thinning of volcanics is not reflected in the f_0 values, as well as borehole S1, which shows the largest deviation from the best-fit curve.

Assuming the quarter-wavelength approximation for the resonant frequency of the volcanic layer above bedrock, an average V_{SZ} velocity of ~640 m/s can be derived from Eq. (5) for the volcanics, slightly higher than the average value derived for the volcanics from the 4 arrays (~550 m/s). This suggests that we most probably have local variations of the Vs structure within the pyroclastics, with some areas (most probably borehole S1) exhibiting higher velocities (e.g., at large depths) than those identified in the four arrays, leading to a somewhat higher average Vs value. In Fig. 13 we also present the original data (open circles) and the empirical relation ($H = 81.94 * T_0$) derived from HVSR data collected in several mainly Quaternary Greek sedimentary basins by Chatzis et al. (2018). The comparison suggests that not only the average V_{SZ} value (above bedrock) is much higher for Santorini volcanics, compared to the typical Greek Quaternary sediments (which correspond to a V_{SZ} of ~330 m/s) but that the "blind" application of relations like eq. (5) derived from a different geological environment (as adopted in several studies) can lead to a significant bias of the inferred bedrock depths.

To compute the absolute elevation of the underlying metamorphic basement from sea level, we combined volcanic thicknesses with the local Santorini DEM. Eq. (5) was used to determine the total pyroclastic thickness at all sites where f_0^{HVSR} was measured. Flat HVSR curves as well as bedrock sites (according to the geological map) were assigned zero

thickness. While the direct use of the available f_0^{HVSR} data and Eq. (5) allowed us to recover the thickness of pyroclastic deposits above the metamorphic basement in central-southern Santorini, it is interesting to also study the observed HVSR data, as the shape and the observed maximum amplitude of the curves reveal additional information for the geological interpretation of the results. For this reason, we first study the resulting metamorphic basement geometry and the corresponding HVSR curve patterns along three cross-sections presented in Figs. 14–16 (locations shown in Fig. 2). For each section we also show indicative HVSR curves (recorded on or very close to the profile) at the top.

Cross-section A-A' (Fig. 14) samples the main basement formations crossing Santorini and passes through Athinios port, Megalochori basin, and Mt. Profitis Ilias. The stratigraphy of the nearby borehole S1 is also projected onto the cross-section. Sharp HVSR peaks (e.g., HVSR-01 and 02) are observed for the entire Megalochori basin, with $f_0 \sim$ 1.2-2 Hz and large A_0^{HVSR} values (between 4 and 9) due to the high impedance contrast of the pyroclastics with the metamorphic basement. Higher f_0 values (locally $f_0 \sim$ 4 Hz) have been observed very close to the bedrock. Outcropping basement formations are observed both along the Athinios caldera wall, as well as at the Profitis Ilias, where typical, flat HVSR curves are seen (HVSR-04 and -05).

Cross-section (B-B') runs parallel to the caldera wall and then across the flank of Mt. Profitis Ilias into the Perissa basin, extending from Fira through Pirgos to Ag. Efraim (Fig. 15). For comparison, a simplified geological stratigraphy of the caldera wall between HVSR stations 12 and 14 is shown in the bottom image. Very low f_0 values (<0.5 Hz, e.g., 11, 12 and 13 HVSRs) are observed over the deep Fira basin, where the inferred volcanic thicknesses exceed 300 m. At these sites we observe a second HVSR peak, labelled f_1, at 0.75-1 Hz that has a lower maximum amplitude ($A_1^{HVSR} < 3$) compared to the fundamental peak. The caldera wall stratigraphy shows that at these locations, lavas of the first explosive cycle lie between the basement and the upper pyroclastic deposits. This suggests that this secondary HVSR peak is due to the contrast between overlying younger volcanics and these deep, more competent (high Vs, high density) formations, while f_0^{HVSR} still reflects the impedance velocity contrast between the volcanics and the metamorphic basement. To obtain thicknesses for both layers we applied eq. (5) to the
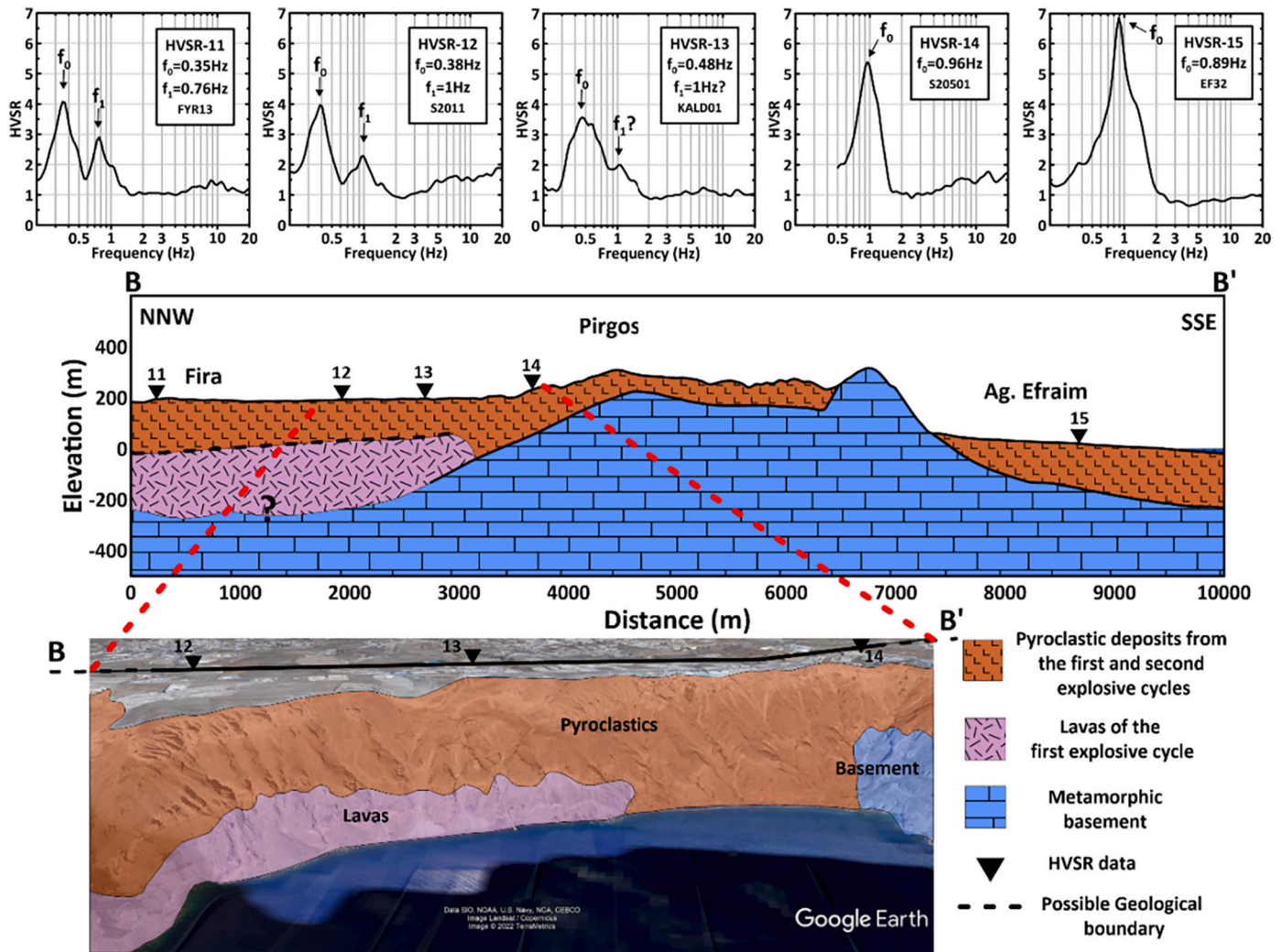
Fig. 15. (Top) Same as Fig. 14 for cross-section B-B′ along Fira, Pirgos, and Ag. Efraim/Perissa basin (see Fig. 2). (Bottom) Simplified stratigraphy of the caldera wall along the same cross-section between stations HVSR-12 and HVSR-14 (geology adapted from Druitt et al., 1999).

f_1 and f_0 values. While the thickness for the shallower contact between pyroclastics and lavas is likely reliable, the depth for the deeper lavas to basement interface (~400-450 m) beneath Fira should be considered a minimum estimate, since the average velocity of the pyroclastics and lava package is expected to be larger than the 640 m/s inferred from eq. (5). To the SSE near Pirgos and in the basin between Pirgos and the basement outcrop, a significant f_0 increase, with single sharp peaks (e.g., HVSR-14) similar to those in Fig. 14, is observed (HVSR-13 and -14). Finally, the deep Perissa basin exhibits sharp HVSR peaks ($A_0^{HVSR} \sim$ 3.5–8), e.g., HVSR-15, due to the pyroclastics to basement contrast.

The last cross-section (C-C′) in Fig. 16 crosses the Pirgos and the Kamari basins, includes boreholes S2 and S3 and extends from Agia Anna through Pirgos to Monolithos. From borehole S3 (HVSR-23) to Pirgos and the Kamari basin (between Pyrgos and Monolithos), sharp HVSR peaks (HVSR-23 and -24) identify the pyroclastics to the basement interface, as also seen in borehole S3 and the previous cross-sections. However, in the SW, from HVSR-22 towards Agia Anna (borehole S2, HVSR-21), the HVSR amplitudes drop to $A_0^{HVSR} < 3$ and the HVSR curves are more complex. This drop is clearly due to the moderate impedance contrast between the pyroclastics and the older Akrotiri lavas and tuffs, that overlay the basement (see borehole S2). In addition, to the northeast of station HVSR-24, where the Monolithos bedrock outcrop is located, complex (mostly double-peaked and low A_0^{HVSR}) HVSR curves are observed (e.g., HVSR-25). Such curves suggest a more-complex 3D

geology (e.g., additional formations beneath the pyroclastics, similar to the Fira area) and smaller impedance contrasts between the subsurface formations.

4. Discussion - conclusions

In Figs. 17 and 18 we show the spatial variation of pyroclastic deposits thickness and the pre-Alpine metamorphic basement elevation, respectively, derived from eq. (5) and the f_0^{HVSR} values. In the Fira area (in the North) the thickness shown corresponds to a minimum estimate due to the presence of the deeper, first cycle volcanic formations (see Fig. 15). In the southwestern part of the model, the pyroclastics are underlain by the sub-surface Akrotiri formations, placed between the metamorphic basement and the pyroclastic volcanism in this area (see Fig. 16). We have excluded the broader Monolithos area from the plot, despite the large number of HVSR data collected in this area, since the geological interpretation of the complex HVSR curve pattern is inconclusive (see Fig. 16). For the metamorphic basement morphology (Fig. 18), we only used results where a clear, single/prominent HVSR peak was identified, consistent with the presence of low-density/low-velocity pyroclastics on top of the metamorphic basement.

Both final maps show that several deep basins exist around the metamorphic basement of Profitis Ilias and Gavrilos mounts, most of them exceeding 200 m in depth, such as the Perissa basin in the
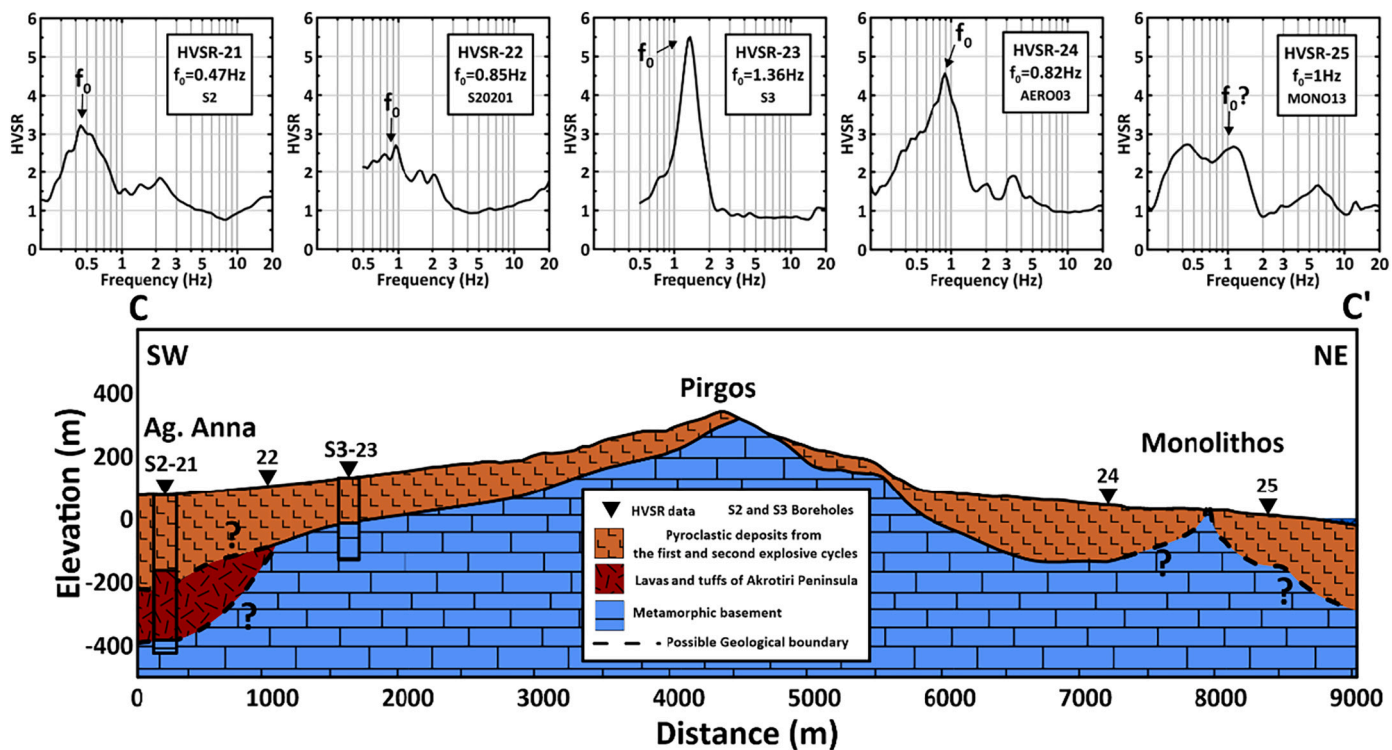
Fig. 16. Same as Fig. 14 for cross-section C-C′ (Ag. Anna to Pirgos and Monolithos, see Fig. 2), with boreholes S2 and S3 superimposed on the cross-section.
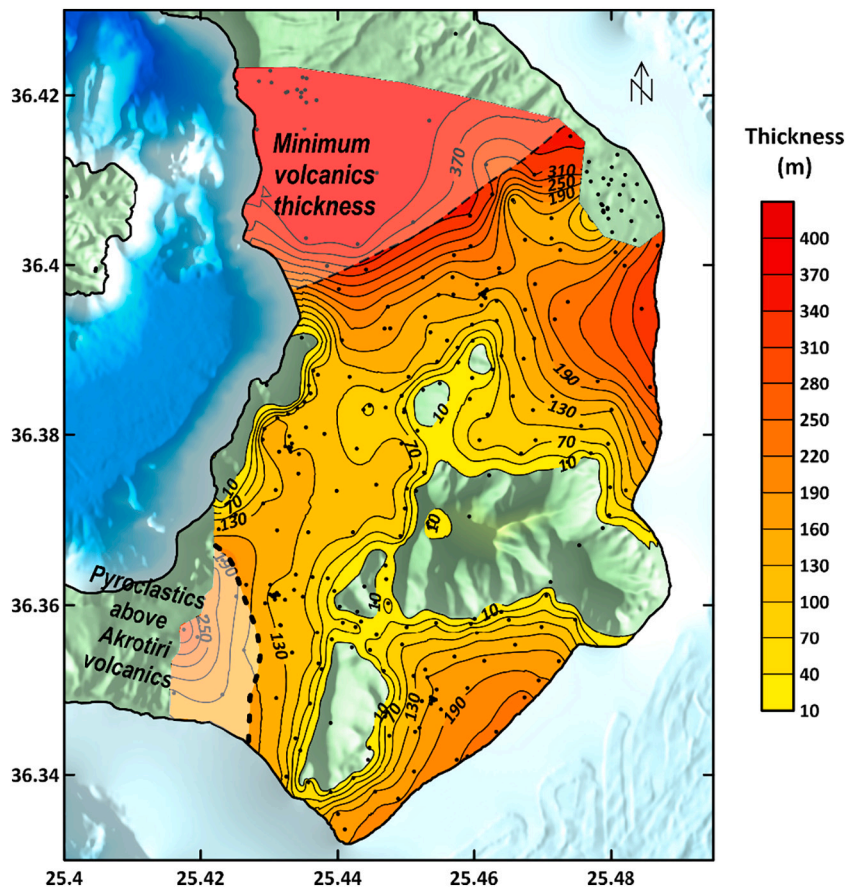

Fig. 17. Thickness of pyroclastic deposits above the metamorphic basement in central-southern Santorini, determined in this study (see text for details).
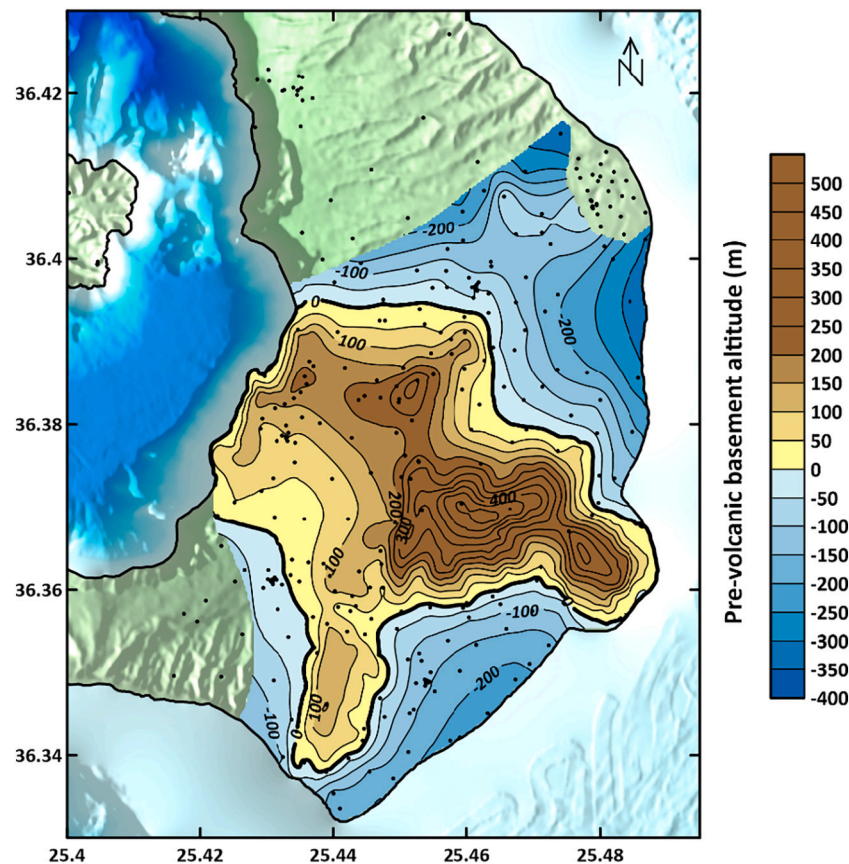
Fig. 18. Pre-Alpine metamorphic basement elevation above sea level in central-southern Santorini. The thick solid line depicts the equivalent present metamorphic island shoreline, with all volcanic deposits removed.

southeast. In addition, an almost "flat" basin plateau is observed to the west of the Profitis Ilias (Megalochori area) towards the Athinios port, with thicknesses ranging from 70 to 130 m. This is the only area where the metamorphic basement is located above sea level. In the remaining part of Santorini island (e.g., Fira, Kamari, Perissa, etc.) the basement is found below sea level and was raised above sea level by the pyroclastic deposits and volcanic material that has accumulated as result of volcanic activity during the last ~650Kyr.

The results presented in Figs. 17 and 18 share common features with previous geophysical studies but also provide new information on the local geology. The metamorphic Santorini "coastline" pattern presented in Fig. (18) is similar to the topography of the pre-Alpine basement proposed by Tzanis et al. (2020) based on gravity data. However, several smaller-scale features are significantly different. For example, as shown in Figs. 16 and 17, the Akrotiri volcanics have a sub-surface continuation to the east, lying between the metamorphic basement and the surface pyroclastics. More specifically, they extend roughly 2.5 km to the east of their visible surface boundary (which was adopted as their westernmost limit by Tzanis et al., 2020), as seen from the comparison of Fig. 2 (surface geology) and Fig. 17. Moreover, while Tzanis et al. (2020) suggest that the thickness of pyroclastics in the Megalochori area between Profitis Ilias and Athinios is almost negligible, we demonstrate the presence of a thick (~70-130 m) pyroclastics layer on top of a local metamorphic basement "plateau".

To the north of Mesaria and Monolithos (roughly the ENE-WSW lineament depicted in Fig. 17), there is a very deep basin in the broader Fira area with volcanics exceeding 400 m thickness. This fault-like boundary is in good agreement with the larger-scale tomographic results of Heath et al. (2019), who identified a similar transition from the high P-velocity basement to a deep, low P-velocity volcanic basin in northern Santorin in their tomographic plots at shallow depths (0-1 km depth). It should be noted that because of the different scales of the studies, the smaller-scale basins delineated in this work (e.g., Perissa area) cannot be identified in the P-wave tomography results due to the sparsity of recording stations and sparse shallow ray coverage.

There are several open questions and local discrepancies that merit additional research. For example, while the bedrock depth of borehole S3 is in good agreement with the proposed scaling (eq. 5) (Fig. 13), the bedrock depth in borehole S1 is significantly larger that the HVSR pre-diction (Fig. 14). This bias may be due to lateral velocity variations within the pyroclastic formations or to the intrinsic limitation of the 1D HVSR approach in a strongly varying 2D/3D structure. Moreover, despite the dense data coverage in the Monolithos bedrock outcrop area (see Figs. 1 and 2), the complex HVSR curves with relatively low f_0^{HVSR} values observed in this area are not consistent with the simple bedrock outcrop geometry shown schematically in Fig. 16. It should be noted that to model the gravity field in the same area Tzanis et al. (2020) employed a thick pyroclastic layer (>100 m) and removed the local bedrock horst at Monolithos. This suggests that the Monolithos bedrock outcrop may be a localized, isolated feature (e.g., a detached basement fragment within the pyroclastics) and not a coherent uplift of the metamorphic basement.

Our results show that the combination of the "standard" HVSR technique with the inversion of surface wave dispersion curves (both passive and active) and the available geological constraints provided new information on the detailed geology of central-southern Santorini. The large number of HVSR measurements, as well as the spatial co-herency of the recovered HVSR curves allowed us to recover the pre-Alpine basement geometry. This geometry is one of the main control-ling factors for the structure of the overlying volcanics, since the pre-existing topography of the metamorphic Santorini basement affects the flow paths and the resulting accumulation pattern of volcanic

materials throughout the history of the Santorini volcano.

The presented results provide a solid basis for the development of a local site amplification model for the central-southern part of Santorini. The main contribution is the bedrock depth (Fig. 18), which controls the fundamental frequency of the local transfer functions. If we consider the very large A_0^{HVSR} values locally observed in Fig. 7, as well as the inference from experimental data (e.g., Haghshenas et al., 2008) that A_0^{HVSR} corresponds to an average lower estimate of the actual spectral amplifications, it can be expected that several locations in Santorini will exhibit spectral amplifications larger than 8, at least close to the fundamental frequency (mainly in the range 0.5-5 Hz). Furthermore, the results obtained for the V_S velocity structure shown in Fig. 10, as well as in the Appendix 0, verify the presence of relative thin, low V_S surficial formations. These softer, mainly Minoan, deposits can clearly generate significant amplifications at higher frequencies (5–20 Hz), that are closer to the fundamental frequency of the typical building inventory of Santorini. It can be suggested that the combined effect of such amplifications due to the local geology, as well as the topographic effect which has been shown to be important for Santorini (e.g., Kkallas et al., 2018) can result in a significant aggravation of seismic motions for the majority of Santorini settlements that built on volcanics, in comparison to the reference bedrock motions. Additional related research, involving seismic amplification studies (e.g., from earthquake records), smaller (local) scale geophysical exploration, and 3D wave propagation modeling can benefit from the developed bedrock and velocity models.

CRediT authorship contribution statement

Nikos Chatzis: Conceptualization, Methodology, Software, Validation, Formal analysis, Investigation, Resources, Data curation, Writing – original draft, Writing – review & editing, Visualization. **Costas Papazachos:** Conceptualization, Methodology, Validation, Formal analysis, Investigation, Resources, Data curation, Writing – original draft, Writing – review & editing, Visualization, Supervision, Project administration, Funding acquisition. **Nikos Theodoulidis:** Methodology, Investigation, Resources, Writing – original draft. **Panagiotis Hatzidimitriou:** Investigation, Writing – original draft. **Georgios Vougioukalakis:** Conceptualization, Validation, Investigation, Resources, Funding acquisition. **Michele Paulatto:** Investigation, Resources, Data curation, Writing – original draft. **Ben Heath:** Investigation, Resources, Data curation. **Emilie Hooft:** Conceptualization, Investigation, Resources, Data curation, Writing – original draft, Supervision, Project administration, Funding acquisition. **Douglas Toomey:** Conceptualization, Investigation, Resources, Data curation, Writing – original draft, Supervision, Project administration, Funding acquisition. **Marios Anthymidis:** Methodology, Software, Investigation, Resources, Data curation. **Chrisa Ventouzi:** Methodology, Software, Resources, Data curation.

Declaration of Competing Interest

Nikos Chatzis reports financial support, equipment, drugs, or supplies, and travel were provided by Aristotle University of Thessaloniki. Nikos Chatzis reports financial support was provided by Greek State Scholarships Foundation. Nikos Chatzis reports equipment, drugs, or supplies and travel were provided by Institute for the Study of Santorini Volcano.

Data availability

Data will be made available on request.

Acknowledgements

Appendix A

Results from the joint inversion of dispersion curve (DC) and fundamental frequency (f_0) for sites MEG, SXL and KTS (see Fig. 3 for locations). The notation is the same as in Fig. 10.
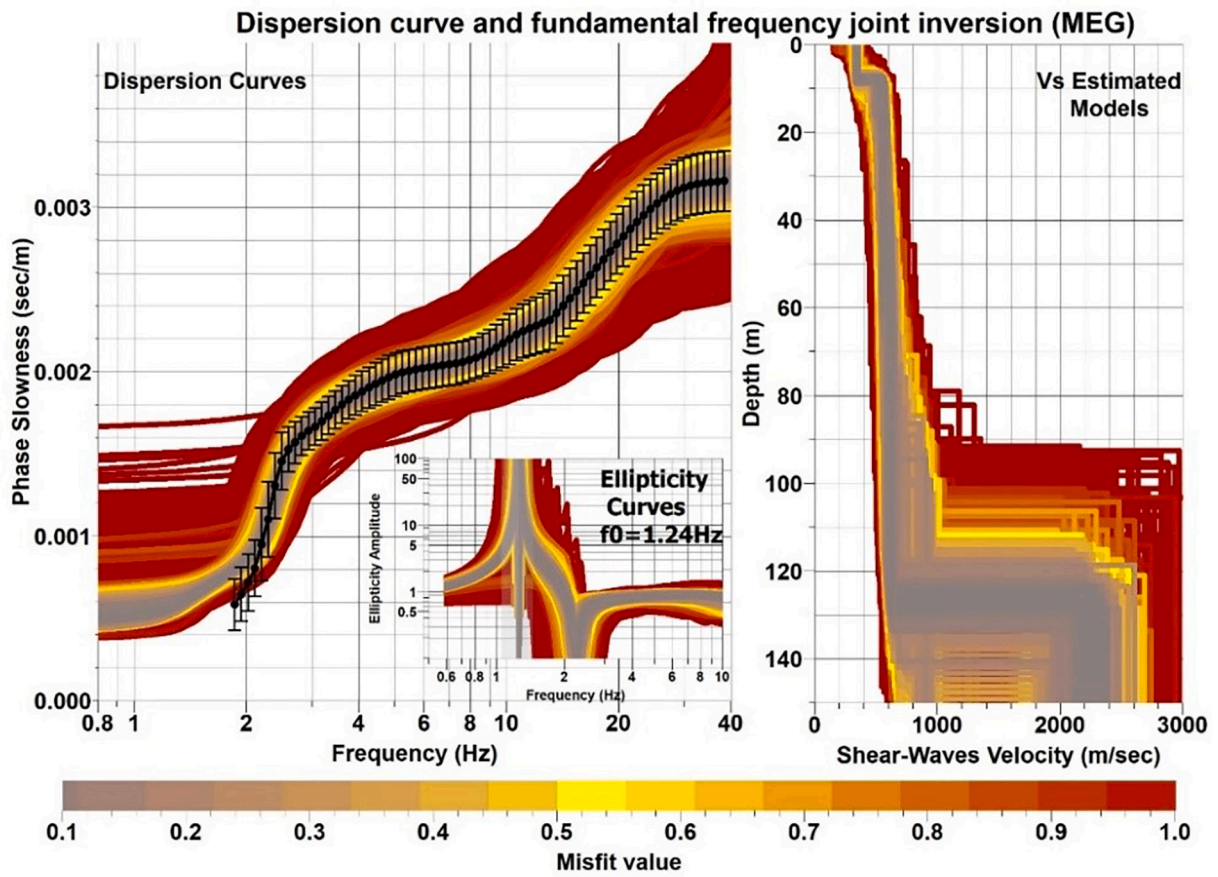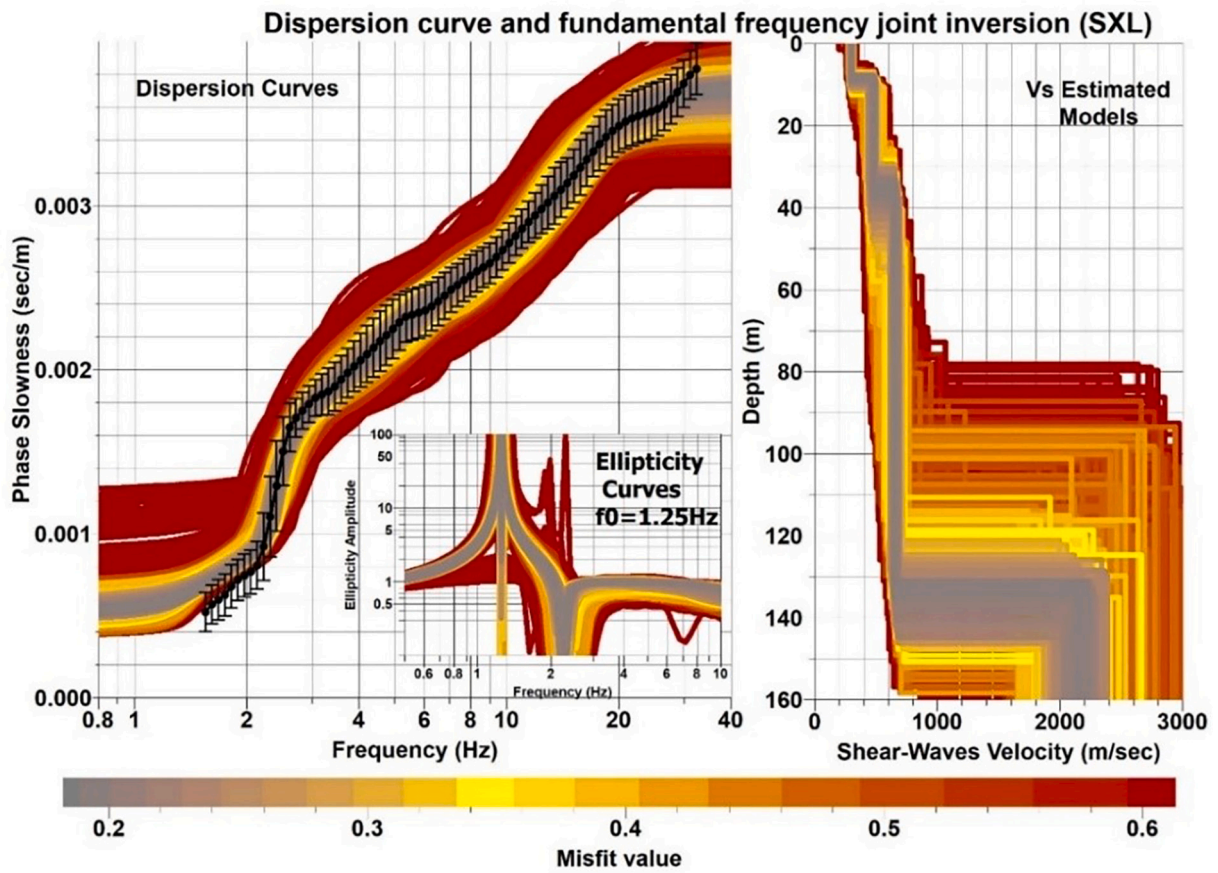
Fig. A1. Same as Fig. 10 for site MEG.

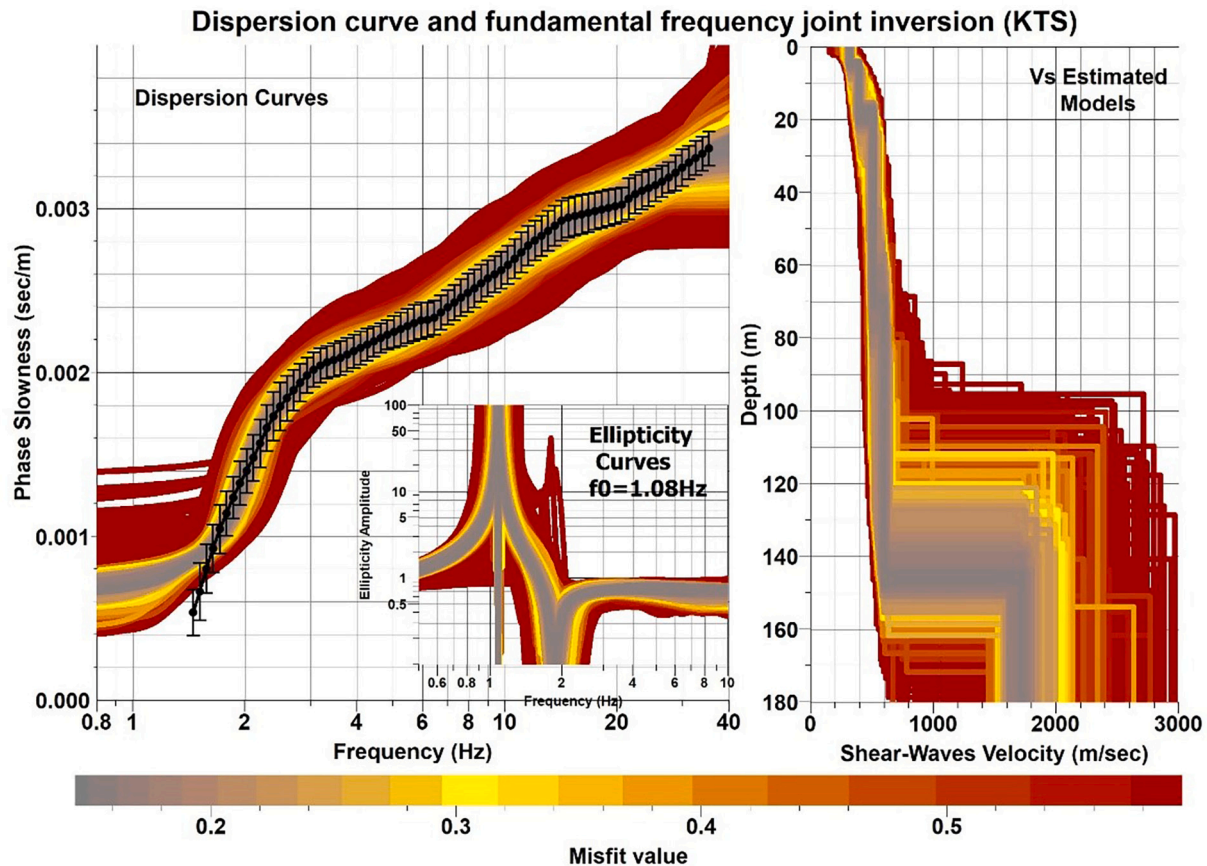**Fig. A2.** Same as Fig. 10 for site SXL.

Fig. A3. Same as Fig. 10 for site KTS.

References

Aki, K., 1957. Space and time spectra of stationary stochastic waves, with special reference to microtremors. Bulletin of the Earthquake Research Institute 35, 415–456.

Altherr, R., Schliestedt, M., Okrusch, M., Seidel, E., Kreuzer, H., Harre, W., Lenz, H., Wendt, I., Wagner, G.A., 1979. Geochronology of high-pressure rocks on Sifnos (Cyclades, Greece). Contrib. Mineral. Petrol. 70 (3), 245–255.

Andriessen, P.A.M., Boelrijk, N.A.I.M., Hebeda, E.H., Priem, H.N.A., Verdurnen, E.T., Verschure, R.H., 1979. Dating the events of metamorphism and granitic magmatism in the Alpine Orogen of Naxos (Cyclades, Greece). Contrib. Mineral. Petrol. 69 (3), 215–225.

Andriessen, P.A.M., Banga, G., Hebeda, E.H., 1987. Isotopic age study of pre-Alpine rocks in the basal units on Naxos, Sikinos and Ios, Greek Cyclades. Geologie en Mijnbouw 66 (3), 3–14.

Arai, H., Tokimatsu, K., 2005. S-wave velocity profiling by joint inversion of microtremor dispersion curve and horizontal-to-vertical (H/V) spectrum. Bull. Seismol. Am. 95 (5), 1766–1778.

Baillie, M.G., Munro, M.A., 1988. Irish tree rings, Santorini and volcanic dust veils. Nature 332 (6162), 344–346.

Bard, P.Y., 2008. The H/V technique: capabilities and limitations based on the results of the SESAME project. Bull. Earthq. Eng. 6 (1), 1–2.

Bohnhoff, M., Rische, M., Meier, T., Becker, D., Stavrakakis, G., Harjes, H.P., 2006. Microseismic activity in the Hellenic Volcanic Arc, Greece, with emphasis on the seismotectonic setting of the Santorini–Amorgos zone. Tectonophysics 423 (1–4), 17–33.

Bonnefoy-Claudet, S., Cotton, F., Bard, P.Y., Cornou, C., Ohrnberger, M., Wathelet, M., 2006a. Robustness of the H/V ratio peak frequency to estimate 1D resonance frequency. In: Proceedings of the 3rd International Symposium on the Effects of Surface Geology on Seismic Motion, Grenoble, France, 30 August – 1 September 2006, Paper Number: 85 (10pp).

Bonnefoy-Claudet, S., Cotton, F., Bard, P.Y., 2006b. The nature of noise wavefield and its applications for site effects studies: A literature review. Earth Sci. Rev. 79 (3–4), 205–227.

Bonnefoy-Claudet, S., Köhler, A., Cornou, C., Wathelet, M., Bard, P.Y., 2008. Effects of love waves on microtremor H/V ratio. Bull. Seismol. Soc. Am. 98 (1), 288–300.

Borcherdt, R.D., 1970. Effects of local geology on ground motion near San Francisco Bay. Bull. Seismol. Soc. Am. 60 (1), 29–61.

Budetta, G., Condarelli, D., Fytikas, M., Kolios, N., Pascale, G., Rapolla, A., Pinna, E., 1984. Geophysical prospecting on the Santorini Islands. Bull. Volcanol. 47, 447–466. https://doi.org/10.1007/BF01961218.

Capon, J., 1969. High-resolution frequency-wavenumber spectrum analysis. Proc. IEEE 57 (8), 1408–1418.

Chatzis, N., Papazachos, C., Theodoulidis, N., Klimis, N., Anthymidis, M., 2018. 1D Vs models by single-station noise data inversion and joint interpretation with independent data. In: 16th Eur. Conf. Earth. Eng., Thessaloniki, paper 11229, 12pp, 18-21 June 2018.

Chávez-García, F.J., Domínguez, T., Rodríguez, M., Pérez, F., 2007. Site effects in a volcanic environment: A comparison between HVSR and array techniques at Colima, Mexico. Bull. Seismol. Soc. Am. 97 (2), 591–604.

Cheng, T., Hallal, M.M., Vantassel, J.P., Cox, B.R., 2021. Estimating Unbiased Statistics for Fundamental Site Frequency using Spatially distributed HVSR Measurements and Voronoi Tessellation. J. Geotech. Geoenviron. 147 (8), 04021068.

Dimitriadis, I., Karagianni, E., Panagiotopoulos, D., Papazachos, C., Hatzidimitriou, P., Bohnhoff, M., Rische, M., Meier, T., 2009. Seismicity and active tectonics at Coloumbo Reef (Aegean Sea, Greece): monitoring an active volcano at Santorini Volcanic Center using a temporary seismic network. Tectonophysics 465 (1–4), 136–149.

Druitt, T.H., 2014. New insights into the initiation and venting of the Bronze-Age eruption of Santorini (Greece), from component analysis. Bull. Volcanol. 76 (2), 1–21.

Druitt, T.H., Edwards, L., Mellors, R.M., Pyle, D.M., Sparks, R.S.J., Lanphere, M., Davies, M., Barreirio, B., 1999. Santorini volcano. Geological Society Memoir 19.

Ehrlich, Y., Regev, L., Boaretto, E., 2021. Discovery of annual growth in a modern olive branch based on carbon isotopes and implications for the Bronze Age volcanic eruption of Santorini. Sci. Rep. 11 (1), 1–11.

Foti, S., Hollender, F., Garofalo, F., Albarello, D., Asten, M., Bard, P.Y., Socco, V., 2018. Guidelines for the good practice of surface wave analysis: a product of the InterPACIFIC project. Bull. Earthq. Eng. 16 (6), 2367–2420.

Friedrich, W.L., Kromer, B., Friedrich, M., Heinemeier, J., Pfeiffer, T., Talamo, S., 2006. Santorini eruption radiocarbon dated to 1627-1600 BC. Science 312 (5773), 548.

Friedrich, W.L., Kromer, B., Friedrich, M., Heinemeier, J., Pfeiffer, T., Talamo, S., 2014. The olive branch chronology stands irrespective of tree-ring counting. Antiquity 88 (339), 274–277.

Fytikas, M., Karydakis, G., Kavouridis, T., Kolios, N., Vougioukalakis, G., 1990. Geothermal research on Santorini. Thera and the Aegean World III 2, 241–249.

Haghshenas, E., Bard, P.Y., Theodulidis, N., 2008. Empirical evaluation of microtremor H/V spectral ratio. Bull. Earthq. Eng. 6 (1), 75–108.

Heath, B.A., Hooft, E.E.E., Toomey, D.R., Papazachos, C.B., Nomikou, P., Paulatto, M., Warner, M.R., 2019. Tectonism and its relation to magmatism around Santorini Volcano from upper crustal P wave velocity. Journal of Geophysical Research: Solid Earth 124 (10), 10610–10629.

Hobiger, M., Bard, P.-Y., Cornou, C., Le, B.-N., 2009. Single station determination of Rayleigh wave ellipticity by using the random decrement technique (RayDec). Geophys. Res. Lett. 36, L14303. https://doi.org/10.1029/2009GL038863.

Höflmayer, F., 2012. The date of the Minoan Santorini eruption: quantifying the "offset". Radiocarbon 54 (3–4), 435–448.

Jolivet, L., Faccenna, C., Huet, B., Labrousse, L., Le Pourhiet, L., Lacombe, O., et al., 2013. Aegean tectonics: Strain localisation, slab tearing and trench retreat. Tectonophysics 597, 1–33.

Kkallas, C., Papazachos, C., Skarlatoudis, A., Anthymidis, M., Ventouzi, C., 2018. Topographic amplification effects on seismic motions: the case of the large (M=7.4) 1956 Amorgos earthquake and its impact in the area of Santorini. In: 16th Eur. Conf. Earth. Eng., paper 10430, Thessaloniki, 18-21 June.

Konno, K., Ohmachi, T., 1998. Ground-motion characteristics estimated from spectral ratio between horizontal and vertical components of microtremor. Bull. Seismol. Soc. Am. 88 (1), 228–241.

Kula, D., Olszewska, D., Dobiński, W., Glazer, M., 2018. Horizontal-to-vertical spectral ratio variability in the presence of permafrost. Geophys. J. Int. 214 (1), 219–231.

Le Pichon, X., Angelier, J., 1979. The Hellenic arc and trench system: a key to the neotectonic evolution of the eastern Mediterranean area. Tectonophysics 60 (1–2), 1–42.

Leyton, F., Ruiz, S., Sepúlveda, S.A., Contreras, J.P., Rebolledo, S., Astroza, M., 2013. Microtremors' HVSR and its correlation with surface geology and damage observed after the 2010 Maule earthquake (Mw 8.8) at Talca and Curicó, Central Chile. Engineering geology 161, 26–33.

Manning, S.W., Höflmayer, F., Moeller, N., Dee, M.W., Ramsey, C.B., Fleitmann, D., Higham, T., Kutschera, W., Wild, E.M., 2014. Dating the Thera (Santorini) eruption: archaeological and scientific evidence supporting a high chronology. Antiquity 88 (342), 1164–1179.

Mercier, J.L., Sorel, D., Vergely, P., Simeakis, K., 1989. Extensional tectonic regimes in the Aegean basins during the Cenozoic. Basin Res. 2 (1), 49–71.

Moisidi, M., Vallianatos, F., Kershaw, S., Collins, P., 2015. Seismic site characterization of the Kastelli (Kissamos) Basin in Northwest Crete (Greece): assessments using ambient noise recordings. Bull. Earthq. Eng. 13 (3), 725–753.

Nakamura, Y., 1989. A method for dynamic characteristics estimation of subsurface using microtremor on the ground surface. Railway Technical Research Institute, Quarterly Reports 30 (1).

Nardone, L., Maresca, R., 2011. Shallow velocity structure and site effects at Mt. Vesuvius, Italy, from HVSR and array measurements of ambient vibrations. Bull. Seismol. Soc. Am. 101 (4), 1465–1477.

Nogoshi, M., Igarashi, T., 1971. On the amplitude characteristics of microtremor (part 2). J. Seism. Soc Jpn 24, 26–40.

Panzera, F., D'Amico, S., Colica, E., Viccaro, M., 2019. Ambient vibration measurements to support morphometric analysis of a pyroclastic cone. Bull. Volcanol. 81 (12), 1–11.

Papadopoulos, I., Papazachos, C., Savvaidis, A., Theodoulidis, N., Vallianatos, F., 2017. Seismic microzonation of the broader Chania basin area (Southern Greece) from the joint evaluation of ambient noise and earthquake recordings. Bull. Earthq. Eng. 15 (3), 861–888.

Papastamatiou, J., 1956. Sur l'age des calcaires cristallines de l'ile de Thera (Santorin). Bull. Geol. Soc. Greece 3, 104–113.

Papazachos, B.C., Papazachou, C., 2003. The Earthquakes of Greece. Ziti publications, Thessaloniki, Greece (286 pp. in Greek).

Papazachos, B.C., Papaioannou, C.A., Papazachos, C.B., Savaidis, A.S., 1997. *Atlas of Isoseismal Maps for Strong Shallow Earthquakes in Greece and Surrounding Area* (426BC-1995). Ziti publications, Thessaloniki (176pp).

Park, C.B., Carnevale, M., 2010. Optimum MASW survey—Revisit after a decade of use. In: GeoFlorida 2010: Advances in Analysis, Modeling & Design, pp. 1303–1312.

Park, C.B., Miller, R.D., Xia, J., 1999. Multichannel analysis of surface waves. Geophysics 64 (3), 800–808.

Perissoratis, C., 1995. The Santorini volcanic complex and its relation to the stratigraphy and structure of the Aegean arc, Greece. Mar. Geol. 128, 37–58.

Piper, D.J.W., Perissoratis, C., 2003. Quaternary neotectonics of the South Aegean arc. Mar. Geol. 198, 259–288.

Piper, D.J.W., Pe-Piper, G., Perissoratis, C., Anastasakis, G., 2007. Distribution and chronology of submarine volcanic rocks around Santorini and their relationship to faulting. Geol. Soc. Lond., Spec. Publ. 291, 99–111.

Skarpelis, N., Liati, A., 1990. The prevolcanic basement of Thera at Athinios: Metamorphism. Plutonism and mineralization. In: Hardy, D.A. (Ed.), Thera and the Aegean World III. 2. The Thera Foundation, London, pp. 172–182.

Tataris, A.A., 1964. The Eocene in the semimetamorphosed basement of Thera island. *Bulletin of the Geological Society of Greece,* III 1, 232–238.

Torrese, P., Rossi, A.P., Unnithan, V., Pozzobon, R., Borrmann, D., Lauterbach, H., et al., 2020. HVSR passive seismic stratigraphy for the investigation of planetary volcanic analogues. Icarus 351, 113970.

Tzanis, A., Chailas, S., Sakkas, V., Lagios, E., 2020. Tectonic deformation in the Santorini volcanic complex (Greece) as inferred by joint analysis of gravity, magnetotelluric and DGPS observations. Geophys. J. Int. 220 (1), 461–489.

Wathelet, M., 2005. Array recordings of ambient vibrations: surface-wave inversion. PhD Diss., Liége University 161 (185pp).

Wathelet, M., 2008. An improved neighborhood algorithm: Parameter conditions and dynamic scaling. Geophys. Res. Lett. 35, 9.

Wathelet, M., Jongmans, D., Ohrnberger, M., Bonnefoy-Claudet, S., 2008. Array performances for ambient vibrations on a shallow structure and consequences over V s inversion. J. Seismol. 12 (1), 1–19.

Wathelet, M., Chatelain, J.L., Cornou, C., Giulio, G.D., Guillier, B., Ohrnberger, M., Savvaidis, A., 2020. Geopsy: A user-friendly open-source tool set for ambient vibration processing. Seismol. Res. Lett. 91 (3), 1878–1889.

Yilmaz, O., 1987. Seismic Data Processing, 2. Society of Exploration Geophysicists, Tulsa, Oklahoma (526 pp).